Master of Science Thesis in Quaternary Geology and Palaeoclimatology

Crevasses on Svalbard Glaciers: Distribution and Dynamic Controls

Ingunn Farsund

June, 2015

Department of
Earth Science
University of Bergen,
UiB
Norway

Department of
Arctic Geology
University Centre in
Svalbard, UNIS
Norway

Abstract

Crevasses play a key role in understanding a wide range of glaciological processes, but the current understanding is mainly based on a few key studies. Recent years, studies on crevasse formation have been motivated by the understanding of processes of calving and the break up of ice shelves. Dynamics of glaciers can help us to reconstruct long-term environmental changes and describe a glaciers response to climate changes. In addition to the glaciological perspective, crevasses can be major hazard to travelers. Glaciers are important travel routes on Svalbard, but currently there are no systematic data on their distribution or their relationship to glaciological variables.

From ground truth measurements of crevasse positions and crevasse widths on Borebreen and Tunabreen, and manual mapping of crevasses in ArcMap, TerraSAR-X images are confirmed to be a suitable tool for defining crevasse areas on glaciers. However, there are some restrictions to the method based on the variations of backscatter for different glacier surface conditions. This can lead to an underestimation of the crevasse area extent. Delineation of the crevasse area limit line on 32 images in a 22-day cycle in the period from February 9th 2013 to April 1st 2015, shows that the terminal crevasse field of Tunabreen is migrating up-glacier during spring and summer, and stabilizes during winter. This pattern coincides with the pattern of retreat and still stand or advance of the glacier front during the same time period.

By using velocity maps and strain rate maps based on feature tracking from two TerraSAR-X images in a 11-day cycle, it was aimed to find threshold velocity and strain rate for crevasse opening. The velocity maps used only contain velocity information in the lower part of the terminal crevasse field on Tunabreen, and no velocity was detected within the upper part of the crevasse field. Values of the 1st principal strain rate in the upper crevasse area and along the crevasse area limit line could indicate a threshold strain rate for crevasse opening between 0.1 and 0.2 $\text{day}^{-1} \times 10^{-3}$. The resolution and quality of the data used is considered to be too low to define and confirm this as a strain rate threshold for crevasse opening.

The velocity mapping produced by feature tracking of TerraSAR-X images only detects velocity in about half the size of the mapped terminal crevasse field on Tunabreen. When applying the method to the fast-flowing glacier Austre Torellbreen, it is seen that the area of detected velocity is almost equal in extent to the mapped crevasse area. In a safety perspective, crevasse maps based on TerraSAR-X data give a more accurate indication of potential hazardous areas compared to velocity maps.

Acknowledgements

First of all I would like to thank my supervisors. Thank you, Doug Benn (The University Centre in Svalbard), for giving me the opportunity to spend two more years on Svalbard working on an interesting project in such beautiful surroundings, and for encouraging and helping me during the last year in the process of writing this thesis. Also, thanks to Atle Nesje, my supervisor at University of Bergen, for your constructive feedbacks and for always replying to my e-mails.

I also owe Adrian Luckman (Swansea University/UNIS) a huge thank you for providing me the important TerraSAR-X images and additional data. Heidi Sevestre, thanks for helping me organize the field work in addition to spend your valuable time teaching me ArcMap. Your comments on the manuscript are also highly appreciated.

Thanks to UNIS logistics for providing boat transport and security equipment needed during the field work. Sille Marie Myreng and David Wrangborg, you did a great job as field assistants, thanks for using your time to carry around equipment and doing measurements on a remote glacier.

During my five years at the University, I have met and worked together with a lot of great people who have made this time of my life memorable in so many ways. Thanks to my fellow students both at UiB and UNIS for all the great days of literature studies, field work, numerous coffee breaks and useful (and not so useful) discussions.

Silje Smith-Johnsen, you have been the best flat- and officemate one could dream of. Thanks for constructive conversations and discussions within our common research field of glaciology, for good motivation and for always making me laugh.

Thank you to Marita Thomassen for providing suggestions and proofreading of the manuscript.

Håvard, thanks for producing figures in MATLAB and for your constructive comments on the manuscript. You are my inspiration and motivation, thank you for always being there for me and reminding me of what comes after.

Last but not least, I would like to thank my family for their support through my entire study and for always making me believe in myself.

Ingunn Farsund

Ingunn Farsund
Longyearbyen, June 2015

CONTENTS

CHAPTER 1

INTRODUCTION

The deformation of glacier ice can form distinctive structures such as crevasses, which may convey information about past and present patterns of strain that are difficult or impossible to obtain by other means. Herzfeld et al. (2004) describes crevasse patterns as “the writings in a glacier’s history book”. Fracturing is also a key role player in a wide range of glaciological processes, including the formation of deep moulins, calving and shearing of ice stream margins (Benn and Evans, 2010). Furthermore, crevasses pose difficulties and dangers for mountaineers and glacier travelers, and “[...] have long inspired tragic tales of travelers who unsuspectedly disappeared into their great depths [...]” (van der Veen, 1999b). Even though crevasses play a key role in understanding a wide range of glaciological processes, their behaviour and development have attracted relatively little attention from glaciologists. The current understanding of crevasses is mainly based on a few key studies, summarized in a review by van der Veen (1999b). Recent years, studies on crevasse formation have been motivated by the understanding of the processes of calving (Benn et al., 2007a) and the break up of ice shelves (Joughin and MacAyeal, 2005).

Crevasses are major hazards for travelers on Svalbard glaciers, but currently there are no systematic data on their distribution or their relationship to glaciological variables. During the winter season, glaciers are important travel routes for both skiing and snow mobiling, but the crevasse fields on the glaciers are not always mapped or well known. Mapping of glaciers and their crevasse fields can be challenging because of their remote location and inaccessibility during the summer season, and the fact that they are often covered by snow in the winter.

This study will try to develop a method to identify terminal crevasse fields from TerraSAR-X satellite data (X-band radar), with ground truthing from field observations. The seasonal variability of the terminal crevasse field will be compared to the terminus fluctuations by mapping a complete annual cycle of radar images. The relationship between the crevasse fields, glacier velocities and glacier surface strain rates will also be investigated using velocity maps and strain rate maps derived from speckle-tracking using 11-day repeat TerraSAR-X data. Synthetic Aperture Radar (SAR) results in high-quality radar images independent on cloud cover and daylight. Thanks to the high spatial and temporal resolution, radar images from the TerraSAR-X satellite are a suitable tool for the observation and monitoring of the glacier surface (Schubert et al., 2010; Schubert et al., 2012).

1.1 Aims and objectives

From the challenges of crevasses, both in a safety perspective and from a glaciological view, the motivation arose to apply recent remote sensing techniques to map and analyze crevasse fields on selected glaciers. In addition, the relationship between crevasse fields, velocity and surface strain rates is of interest, to better understand how the crevasse fields develop. The chosen glaciers are Borebreen, Tunabreen and Austre Torellbreen.

The primary aim of this study is to assess the suitability of TerraSAR-X images in delineating crevasse fields and investigate how the terminal crevasse field is propagating in a complete winter-to-winter annual cycle. Ground truth measurements of crevasse positions and crevasse widths were carried out on Borebreen and Tunabreen to try verifying if the crevasses measured on the glacier surface were possible to map on the TerraSAR-X images, and vice versa. Additionally, mapped TerraSAR-X images can be compared with field measurements to define how wide a crevasse has to be to be picked up in the SAR images. By processing the ground observation data and comparing this to the mapped crevasse fields from the satellite images, it will hopefully be possible to verify the use of TerraSAR-X satellite images as a reliable source when mapping crevasse fields. The findings can be used to better understand glaciological variables in the development of crevasses and migration of crevasse fields. In addition, it will be possible to say if the use of velocity maps and/or crevasse maps based on TerraSAR-X images can be used as a public source for safe glacier travel.

To achieve this aim, five research objectives have been formulated and will be investigated deeper in the following chapters:

1. Use of TerraSAR-X images to map crevasse fields on selected glaciers and compare satellite data with ground data to verify the quality of the data
2. Define glacier front and terminal crevasse field fluctuations through at least one complete annual cycle (winter-to-winter) on Tunabreen.
3. Investigate the relationship between surface strain rates, glacier velocity and the fluctuations of mapped crevasse fields.
4. Determine if the opening of new crevasses can be related to a specific strain rate threshold.
5. Determine if velocity maps or crevasse maps based on TerraSAR-X data can be used to indicate areas of high risk that should be avoided by glacier travelers.

1.2 Thesis structure

This thesis can be divided into four parts:

Part 1

Chapter 1 gives a short introduction into the state of research, the motivation, the aim and research objectives.

Chapter 2 is a summary of relevant background theory needed to understand the following chapters.

Chapter 3 presents the study area of Svalbard as well as a more detailed description of the selected glaciers Borebreen, Tunabreen and Austre Torellbreen.

Part 2

Chapter 4 presents the methods and data used in this study.

Part 3

Chapter 5 presents the results from the study.

Chapter 6 is an interpretation of the presented results and connects the results to the aims and objectives formulated in Chapter 1. The results are also compared with other similar studies.

Part 4

Chapter 7 concludes the study and gives an outlook on what could have been improved and/or added in future studies.

CHAPTER

2

THEORETICAL BACKGROUND

This chapter introduces glaciological concepts relevant to this thesis. The main focus is on stress, strain, crevassing and fractures. In addition, some concepts of remote sensing and radar images will also be presented.

2.1 Glacier dynamics

Glaciers are dynamic stores of water in constant change, and exchanges mass and energy with the atmosphere, hydrosphere and other parts of the earth system. The total glacier mass evolves through time depending on the balance between accumulation and ablation, which in turn depend on climate and local topographic factors. Dynamics of glaciers are the resulting ice processes caused by the interplay of the physical mechanisms causing a glacier to move and forces resisting this movement. Understanding the dynamics of glaciers also help us to reconstruct long-term environmental changes from evidence of past and present glacier fluctuations, and describe a glaciers response to climate changes. (Benn and Evans, 2010).

2.1.1 Stress and strain

Glacier motion occurs in response to stresses arising from the weight of the ice. Stress is a measure of how hard a material is being compressed, stretched or twisted as a result of applied forces, and strain measures the amount of deformation that occurs as the result of stress. Van der Veen (1999a) and Hooke (2005) provide guides to analyze stress and strain in ice.

Stresses on a surface are divided into two different components: normal stress, acting at right angles to the surface, and shear stress, acting parallel to the surface. The stress on a surface consists of two equal and opposite tractions. In the case of normal stresses, the two opposite tractions either press together across the surface (compressive stress), or pull away from it (tensile stress). For shear stresses, the tractions are parallel but act in opposite directions. At the base of a glacier, the normal stress acting on the bed is principally due to the weight of the overlying ice. If the bed is horizontal, the normal stress exerted by any ice column with basal area a_b is:

$$\begin{aligned} \sigma_{xx} &= \rho_i g\,(H \times a_b)\,/\,a_b, \text{ or;} \\ \sigma_{xx} &= \rho_i g H \end{aligned} \tag{2.1}$$

where σ_{xx} is the normal stress acting in the vertical (z) direction, ρ_i is the density of the ice, g is gravitational acceleration and H is the ice thickness.

Strain is the change in shape and dimensions of a material due to stress, and at some critical level of stress, which varies between different material, the result will be permanent deformation or failure. Permanent deformation can take the form of brittle failure or ductile deformation. The two fundamental types of strain are pure shear and simple shear. Pure shear involves flattening and stretching of a material under compressive and tensile deviatoric stresses. Simple shear involves deformation of all the lines drawn through a material except those parallel to the shear plane. The two types of strain and strain rates are explained in Figure 2.1, and more detailed described in Section 2.1.2. The amount of strain experienced by a material is measured by comparing its shape and size before and after deformation. The two ways of measuring strain is strain rate and cumulative strain. Strain rate is the amount of strain that occurs per unit time, whereas cumulative strain refers to the net amount of strain that takes place in a given time interval, and depends on both the rate and duration of strain. Strain rates are defined in terms of velocity gradients, or the relative motion of different parts of a material. In pure shear the velocity gradient is measured along the direction of motion, giving the strain rate in the x direction:

$$\dot{\varepsilon}_{xx} = \frac{\delta u}{\delta x} \tag{2.2}$$

For simple shear, the velocity gradients are measured at right angles to the direction of motion:

$$\dot{\varepsilon}_{xy} = \frac{1}{2}\left(\frac{\delta v}{\delta x} + \frac{\delta u}{\delta y}\right) \tag{2.3}$$

The velocities u and v (motion in the x and y directions, respectively) are measured in metres per year, giving the strain rate $\dot{\varepsilon}$ in units of metres per year per metre, written as yr^{-1}. Glacier motion occurs by strain within the ice or the bed, or by sliding at the interface between the two. The relationship between stress and strain in glaciers and their beds are therefore vital to understand the glacier dynamics and glacial geologic processes.

2.1.2 Crevassing and fractures

The most obvious and hazardous feature of any glacier, and perhaps also the most definitive, are the fractures in its surface. Crevasses are signs of the internal strain rates that occur in the ice mass, and can be used as markers to measure ice velocity, as indicators of basal topography and are important as pathways for englacial

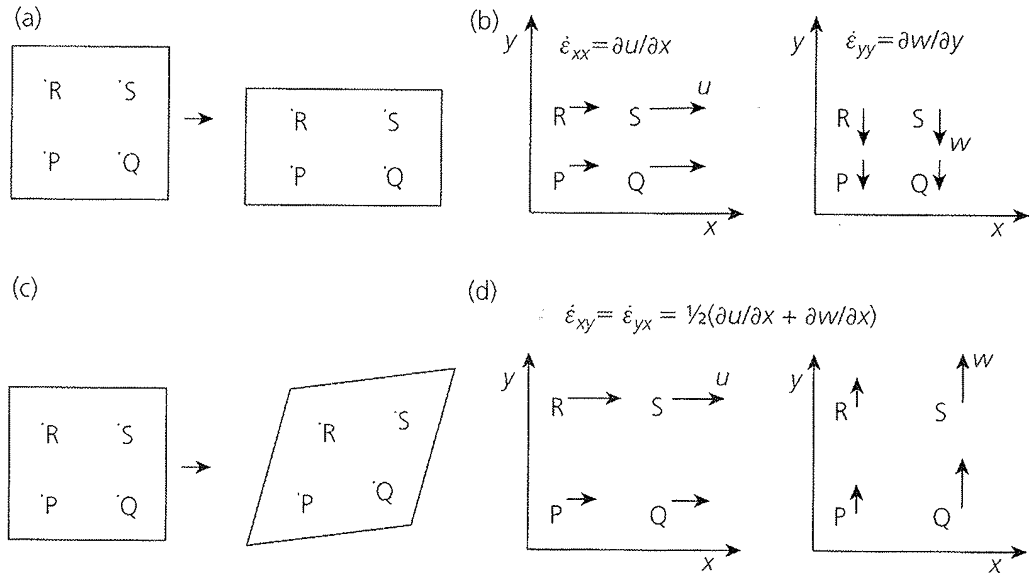

Figure 2.1: Strain rate definitions from Benn and Evans (2010). a) Pure shear where the square is stretched and flattened, but not skewed. b) Strain rates defined in terms of velocity gradients (velocity component u varies in the x direction, and w in the y direction). c) Simple shear where the square is skewed, but not stretched or flattened. d) Strain rate is defined in terms of the gradient of the velocity component$u$ in the y direction, and w in the x direction. Strain is commonly a mixture of pure and simple shear, but can still be resolved in these components.

drainage. Crevasse formation also plays a role in two processes of great importance to glacier dynamics: the calving of icebergs and the penetration of surface water to bed. Models of glaciers as a visco-elastic continuum material work well without considering brittle failure and crevasse research has largely been neglected until the recent interest in calving. Nye (1955) and Nye (1957) presented the first comprehensive model, and much of his work was largely based on work by Hopkins (1844). Van der Veen (1999b) gives a good overview of much of the early crevassing literature.

Crevasses are formed when tensile or compressive stresses exceed the fracture strength of the ice and its ability to deform plastically in response. They may mark acceleration in the ice mass and is often seen in areas of bedrock steepening or obstruction. Crevasses are normally oriented at right angles to the principal tensile stress direction at formation. Later they may be rotated from the original position by changes in glacier flow. This can also close some crevasses and open up others perpendicular to the now prevailing flow direction (Paterson, 1994; van der Veen, 1999a). Crevasses will open up wherever the forces pulling ice apart exceed the strength of the ice, triggering brittle failure. There are three basic ways for crevasses to develop, these are also named as fracture modes (Figure 2.2):

1. **Mode I fracture** (opening mode) occurs as a result of tensile stresses pulling the walls of the crack apart.

2. **Mode II fracture** (sliding mode) occurs in response to shear stresses applied parallel to the crack plane and the crack grows in the same direction as the direction of shear.

3. **Mode III fracture** (tearing mode) also occurs in response to shear stresses, but with crack growth at right angles to the direction of shear.

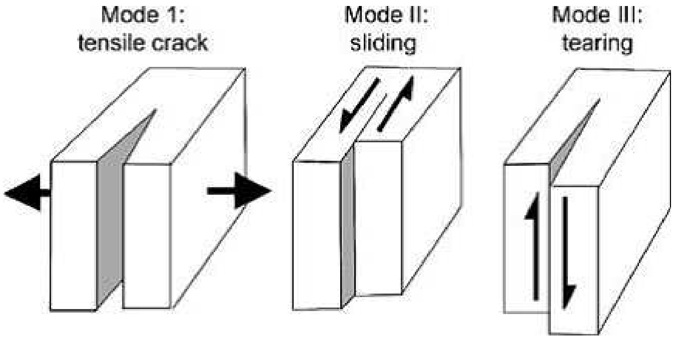

Figure 2.2: Schematic view of the three basic modes of fracturing from Benn et al. (2007a). The first mode is the tensile crack, also named as the opening mode. The second mode is the sliding mode, and the third is the tearing mode.

Crevasses may develop in two or more of the fracture modes simultaneously (mixed-mode fracture), although most analysis are based on the assumption that fracturing is entirely in mode I. The failure criteria for ice have been established from both laboratory experiments and field data, with various and inconsistent results. Results from laboratory experiments are expressed in terms of the applied stress at point of failure (yield stress) or the fracture toughness (Pa $m^{0.5}$). The tensile stresses on glaciers are hard to measure directly, so failure criteria derived from field data are common to express in terms of the threshold strain rate (m m^{-1} yr^{-1}) required for the crevasse initiation (Benn et al., 2007a). Observed threshold strain rates for the initiation of crevassing on glaciers span a wide range. Meier (1958) derived values of around 0.01 yr^{-1} in Greenland, and Hambrey and Muller (1978) recorded crevasses in areas with strain rates as low as 0.004 yr^{-1} on White Glacier, Canada. In the same glacier, they did not record crevasses in areas with strain rates of 0.163 yr^{-1}. Vaughan (1993) reanalyzed published threshold strain rates, which indicated yield stresses varying between 90 kPa and 320 kPa, a variety depending on factors such as ice rheology, temperature, water content, density, crevasse spacing and the influence of complex stress histories (Vaughan, 1993; van der Veen, 1999b; van der Veen, 1998a).

Below the surface of a glacier, any longitudinal tensile stresses that pull the ice apart are at least partly offset by compressive stresses arising from the weight of the overlying ice, illustrated by Equation 2.1. Such compressive stresses increase steeply by depth, so the deeper a crevasse goes, the greater the chance that it will be high enough to offset any tensile stress. Crevasse depth can be defined as the point where the tensile stress tending to open the crevasse is exactly balanced by the compressive stress arising from the weight of the ice. This was used by Nye (1957) to derive the following formula for crevasse depth d for any given surface strain rate:

$$d = \frac{2}{\rho_i g}\left(\frac{\dot{\varepsilon}_{xx}}{A}\right)^{\frac{1}{n}} \tag{2.4}$$

where ρ_i is ice density, g is gravitational acceleration, $\dot{\varepsilon}_{xx}$ is the longitudinal strain rate and A and n are the flow law parameters. Because ice overburden pressure increase rapidly downwards, crevasses may exceed 25-30 meters in polar regions, where ice is colder and stiffer (Paterson, 1994). Mottram and Benn (2009) found that measured crevasse depths on Breiðamerkurjökull, Iceland, were generally close to those using equation 2.4. Where crevasses contain water, ice overburden pressures are opposed by water pressure (van der Veen, 1998a). Benn et al. (2007a) proposed a modified form of the Nye crevasse depth model, incorporating the effect of water pressure:

$$d = \frac{1}{\rho_i g}\left[2\left(\frac{\dot{\varepsilon}_{xx}}{A}\right)^{\frac{1}{n}} + \left(\rho_w g d_w\right)\right] \tag{2.5}$$

where d_w is the depth of water in the crevasse and ρ_w is the water pressure. The crevasse will penetrate deeper when adding water, due to the water pressure acting in the same direction as the longitudinal tensile stress that pulls the crevasse apart. If sufficient water is available, the crevasse may be able to propagate through the full thickness of a glacier, and this has implications for penetration of meltwater and iceberg calving processes (Benn et al., 2007b).

Crevasse classification

Crevasses form at right angles to the principal tensile stress direction, as described by Nye (1952) and Paterson (1994). Tensile stresses can arise from applied normal stresses, shear stresses or a combination of the two classified crevasses in plan view as chevron, transverse and splaying (as shown in Figure 2.3).

1. **Chevron crevasses** (Figure 2.3a) are described as linear fractures aligned obliquely upvalley from the margins of a valley glacier towards the centreline. They form in response to simple shear associated with drag at the valley walls.

2. **Transverse crevasses** (Figure 2.3b) are formed by extending flow on the centre line where shear stresses are zero or close to zero and the tensile principle stress is σ_{xx} thus the crevasses trend at right angles to the principal stress (in the y-direction). At the edge of the glacier, shear stresses are exerted by the valley walls, and in combination with σ_{xx} cause the crevasses to make an angle of more than 45° with the side of the glacier. These transverse crevasses are common behind the calving front of tidewater glaciers. When transverse crevasses link up all the way across the front, they form arcuate crevasse patterns often seen behind calving margins.

3. **Splaying crevasses** (Figure 2.3c) form where valley glaciers are subject to compressive flow, and the crevasses are roughly parallel to the flow direction towards the centre and bend outwards to meet the margins at angles of less than 45°.

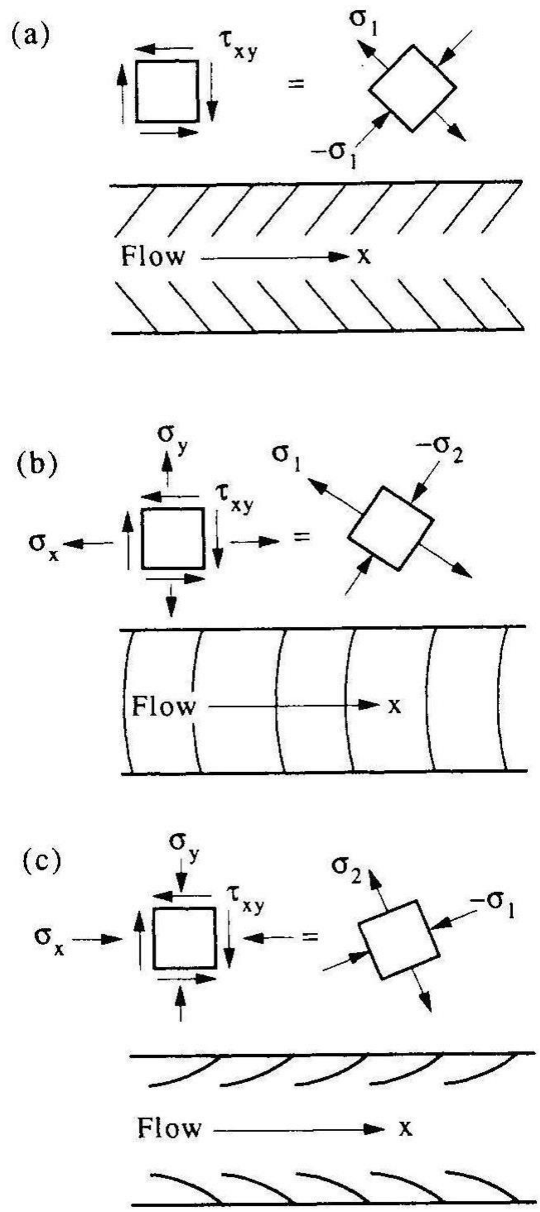

Figure 2.3: Classification of crevasses in plan view, modified by Paterson (1994) from Nye (1952). a) Chevron crevasses formed in response to simple shear associated with drag at the valley walls. b) Transverse crevasses formed by extending flow on the centre line, common behind calving fronts of tide water glaciers. c) Splaying crevasses formed parallel to the flow direction.

Once formed, crevasses will be carried by glacier flow into areas where stress conditions will differ from those which formed them. Crevasses at the margins of valley glaciers and ice streams will tend to rotate because the part nearest the centre line will have the highest velocity. Crevasse patterns can change dramatically at times of changing stress regime, such as when flow is accelerating or decelerating through time (Hambrey and Lawson, 2000). Old deformed crevasses may close, but remain as visible bands of distinct ice or snow, and the orientations of deformed crevasses can be used to infer patterns of ice velocity (Vornberger and Whillans, 1990).

In classical theory (Nye, 1952; van der Veen, 1999b), crevasses are regarded as the Mode I fractures (Figure 2.3) that form normal to the direction of maximum extension. This is determined from the relative values of the three strain rate components. Strain rates in the map plan can be defined in the terms of the surface velocity components U_s and V_s, parallel to the the x (longitudinal) and y (transverse) directions, as seen in the following equations:

$$\dot{\varepsilon}_{xx} = \frac{\delta U_s}{\delta x} \tag{2.6}$$

$$\dot{\varepsilon}_{yy} = \frac{\delta V_s}{\delta y} \tag{2.7}$$

$$\dot{\varepsilon}_{xy} = \frac{1}{2}\left(\frac{\delta V_s}{\delta x} + \frac{\delta U_s}{\delta y}\right) \tag{2.8}$$

When deformation consists of pure shear (Equations 2.6 and 2.7), transverse crevasses will form under longitudinal extension and vice versa. When all deformation is by simple shear (Equation 2.8), crevasses will be oriented at 45° to the direction of shear. Intermediate orientations will occur for different combinations of pure and simple shear (Nye, 1952). Several studies, i.e. Vornberger and Whillans (1990), have made use of this model to infer surface strain patterns and surface stresses from crevasse orientations. However, most field measurements have found that crevasses are not perfectly aligned with the principal stress axes (Whillans et al., 1993). This can be argued too be a reflection of mixed mode failure, such as Mode II fracture superimposed on Mode I fracture (van der Veen, 1999b; van der Veen, 1999a). Another challenge when determining exact relationships between stress fields and crevasse patterns is the advection and rotation of crevasses following their formation (Benn et al., 2007a).

2.1.3 Calving glaciers

Calving events are a consequence of the propagation of fractures in response to stress. When pre-existing or new fractures propagate sufficiently to isolate blocks from the main glacier mass and then fall or float away from the terminus, calving occurs. The location, magnitude and timing of calving events are preconditioned by fracture propagation. The position and form of calving margins reflects the distribution and orientation of former fractures (Benn et al., 2007a). To better understand the calving processes, there are several important issues that have to be addressed. This includes the criteria for fractures to propagate through ice, the control of the rate of fracture propagation, and the control of the depth and the orientation of fractures. These issues are discussed by Benn et al. (2007a), and are also more detailed described in section 2.1.2. The first order controlling calving is the strain rate arising from spatial variations in velocity, which determines the location and depth of surface crevasses (Benn et al., 2007a).

Calving is an important component of the mass budget of many glacier systems, and most of the calving glaciers are fastflowing and undergo sudden changes in speed and terminus position. The understanding of calving glaciers has been developed slowly, due to the diversity of these glaciers. They commonly respond to environmental changes in very different ways, in terms of timing, magnitude and even the sign of terminus position changes. Advance-retreat cycles of calving glaciers also tend to be asymmetrical, with protracted periods of slow advance alternating with short-lived periods of rapid retreat (Meier and Post, 1987). The extent of calving glaciers is of importance because their dynamic behaviour may be partially de-coupled from climate, with factors other than variations in the equilibrium line altitude (ELA) being major controls on the position, and rate of advance or retreat of the calving termini (Benn et al., 2007a; Meier and Post, 1987). Calving glaciers have a potential to contribute to global sea level rise because of their sensitivity to climate changes (Meier and Post, 1987; Rignot et al., 2003). The advance and retreat of calving glaciers involve several dynamic processes. Calving is influenced by the velocity structure of the glacier, and the ice velocity is sensitive to changes in terminus position and force balance (Benn et al., 2007b; Benn et al., 2007a; Meier and Post, 1987).

Tensile stresses associated with along-flow and across-flow gradients in ice velocity are commonly large enough to initiate crevasse formation on glaciers. On many calving glaciers, a combination of dominantly simple shear near the glacier margins and longitudinal extension nearer the centre line creates distinctive arcuate crevasse patterns, which can be mirrored by the form of embayments in the calving front (Benn et al., 2007a). This correspondence suggests that crevasses which have been opened in response to velocity gradients at the glacier scale provide an important first-order control on the position and geometry of calving margins (Powell, 1983). The role of surface strain rates in preconditioning calving is illustrated by the effects of changing strain patterns on surging glaciers (Dowdeswell, 1989).

2.1.4 Surging glaciers

Surging glaciers are glaciers switching between phases of rapid and slow flow on time-scales of a few years to several decades. Surging glaciers are widespread on Svalbard (Dowdeswell et al., 1991; Hagen et al., 1993; Liestøl, 1969). They switch between the period of slow flow known as the quiescent phase when ice builds up in the reservoir area, and the surge or active phase when ice is rapidly transferred from the reservoir area to the receiving area. In a non-surging glacier, there is a balance between accumulation above the equilibrium line altitude (ELA) and the ice flux into the ablation area. Hence, the glacier maintains a near steady-state longitudinal profile. In a surge-type glacier, the ice flux is smaller than the accumulation (balance flux). Thus, the surface gradient gradually increases, in turn causing the basal shear stress to increase. When the shear stress reaches a critical (but unknown) value, a surge can be triggered and sliding increases rapidly. The surge results in a large ice flux from the higher to the lower part of the glacier, usually accompanied by a rapid advance of the glacier front. Often, the glacier is also accompanied by a major subglacial water and sediment flux, and by an increased iceberg production in the case of tidewater glaciers (Hagen et al., 2003a). The surge events occur independently of climatic variations, but the length of the quiescent period is affected by the climate. The morphological evidence of past glacier maximum extent is therefore not necessarily directly linked to climatic conditions but rather to a surge advance (Lefauconnier and Hagen, 1991).

Usually, an initial surge is described by up- and down-glacier propagation of crevasses. This was observed on Bering Glacier by Herzfeld and Mayer (1997), and the up-glacier propagation of fresh surge crevassing continued for at least 12 months after a major water outburst followed by a decreased discharge throughout the following year. Flink et al. (2015) mapped crevasses on Tunabreen and concluded that there was an up-glacier propagation of surface crevasses during its most recent surge between 2002 and 2005.

2.2 Remote sensing in glaciology

Remote sensing techniques use surface crevasses as means of measuring the surface velocity of the glacier by repeat sensing over a specific period of time and matching the same surface features (Howat et al., 2005; Prescott et al., 2003; Rignot and Kanagaratnam, 2006). The techniques include aerial photogrammerty, feature tracking and interferometry. Whillans et al. (1993) discovered the currently inactive ice stream B in Antarctica where the crevasse traces in the shear zone were a clear indication of fast flow in this region in the past. This study showed the use of remote sensing as an important technique to study crevasses and other glaciological features. Measuring glacier velocity and its change through time is an important application to remote sensing in glaciology. One of the common methods is using repeat radar images (SAR) to calculate the glacier velocity. Two pairs of images are used to calculate ascending-pass and descending-pass interferograms. Velocity fields can then be calculated. A combination of radar and optical feature tracking was used by Holt et al. (2013) to investigate the speed-up and fracturing of George VI Ice Shelf in the Antarctic Peninsula. Quincey et al. (2009) used cross-correlation feature tracking to do velocity measurements on Baltoro Glacier, Pakistan.

2.2.1 Synthetic Aperture Radar

A synthetic aperture radar (SAR) is an airborne or spaceborne side-looking radar system that generates high-resolution remote sensing imagery. In SAR imaging, microwave pulses are transmitted by an antenna towards the Earths surface (Figure 2.4a). The microwave energy scattered back to the spacecraft is measured (Figure 2.4b). By using the radar principle, the SAR forms an image by utilizing the time delay of the backscattered signals. The proportion of energy scattered back to the sensor depends on factors like type of land cover, surface roughness, surface water content, slopes and orientation of objects. The cloud penetration property of microwaves makes it possible for a SAR to acquire all-weather images. Being an active remote sensing device, it is also capable of night-time operation.

When interpreting SAR images, the backscatter intensity is important. High backscatter intensity can be caused by a rough or wet surface, while low backscatter intensity can be caused by a smooth or dry surface. High backscatter gives bright images, and low backscatter gives dark images. Very bright areas in the images may appear due to corner reflection or double-bounce effect, when the radar pulse bounces off a horizontal surface and then reflects from a vertical surface on the target back to the sensor. An example of this could be the front of a tidewater glacier.

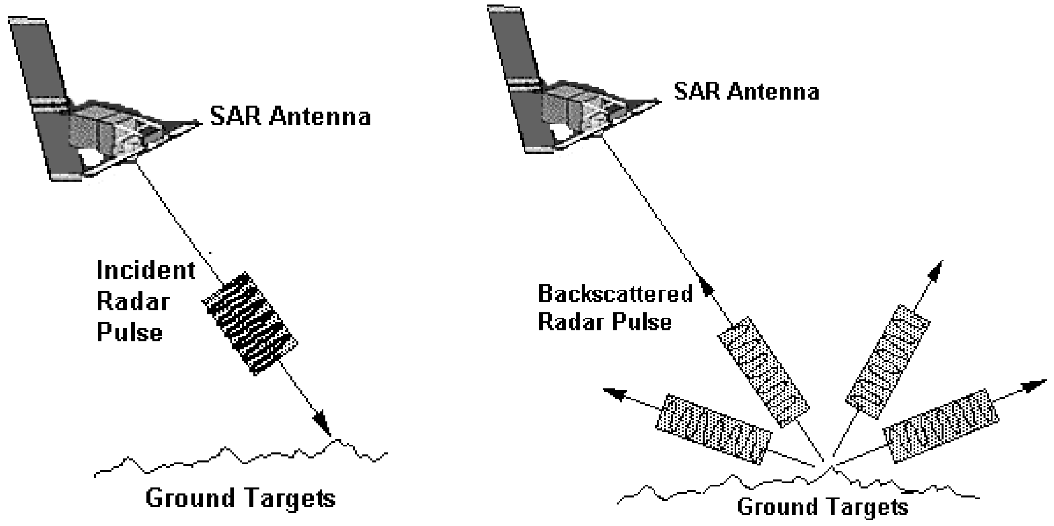

(a) Microwave pulses transmitted by an antenna towards the ground.

(b) Backscattered radar pulses measured by the antenna.

Figure 2.4: Figures illustrating **(a)** the transmitted pulses and **(b)** backscsatter in SAR imaging. Illustrations from Liew (2015).

TerraSAR-X (TSX) is a German Earth observation satellite, built in the context of a public-private partnership between the German Federal Ministry of Education and Research, the German Aerospace Center and Astrium GmbH (Breit et al., 2010). It was launched on 15 June 2007, and the sensor has a nominal lifetime of 5 years, although it is believed to last for at least 7 years. In 2015, it is still running and provides images. The payload of the satellite is an X-band SAR system with a 9.65 GHz centre frequency, included an electronically steerable phased-array antenna and side-looking imaging capability within an off-nadir pivoting range of approximately 20-55°. The satellite has a near-polar dawn/dusk orbit at an altitude of 514 km. With its active radar antenna it is able to produce image data with a spatial resolution in the order of ~1 m, regardless of the weather conditions, cloud cover or absence of daylight. The high spatial resolution and repeat cycle of 11 days, in combination with its extremely high geolocation accuracy (Schubert et al., 2010; Schubert et al., 2012) sets it apart from other civil SAR sensors and opens its use as a feature-tracking data source for glaciers. The stripmap (SM) image mode is the basic imaging mode, with a swath width of ~30 km and pixel spacing of ~2-3 m on the ground.

CHAPTER 3

STUDY AREA

In the following chapter, the geology, climate and present glacial environment of Svalbard are introduced. In addition, the most important glaciological parameters and characteristics of Borebreen, Tunabreen and Austre Torellbreen are presented.

3.1 Svalbard

The Svalbard archipelago is located in the High Arctic between 74° and 81° northern latitude and 10° and 35° eastern longitude (Figure 3.1a). The islands lie between the Fram Strait in the west and the Barents Sea in the east. To the north is the Arctic Ocean. The archipelago comprises four main islands, and the total area is about 61 020 km^2. The largest island is Spitsbergen with an area of 39 044 km^2. As seen on Figure 3.1b, 60% of the archipelago is ice covered (Hagen et al., 1993) and the largest glacier is the ice cap of Austfonna located on the second largest island Nordaustlandet. In general, the landscape is dominated by rugged mountains with steep flanks, but somewhere also by plateau-type terrain (Harland, 1998). The mountain peaks are typically around 1000 m, and the highest peak, Newtontoppen (1713 m), is located in north-eastern Spitsbergen. Deep fjords dominate the landscape on the northern and western part, and tidewater glaciers can be found all along the coast of the island. Along the western and northern coast characteristic strandflats can be found.

3.1.1 Climatic setting

The climate on Svalbard is relatively mild and dry compared to other locations at the same latitude. The West Spitsbergen Current, a branch of the North Atlantic Current, carries warm Atlantic Water into the Arctic Ocean past the West Coast of Spitsbergen. This keeps the waters west and north of Spitsbergen ice free for most of the year (Beszczynska-Möller et al., 2012; Mosby, 1962). Svalbard is also situated in the meeting place in the vicinity for the polar front from the north, and the mild, wet sea air from the south. This creates extreme weather and temperature fluctuations, especially in the winter (Hagen et al., 1993).

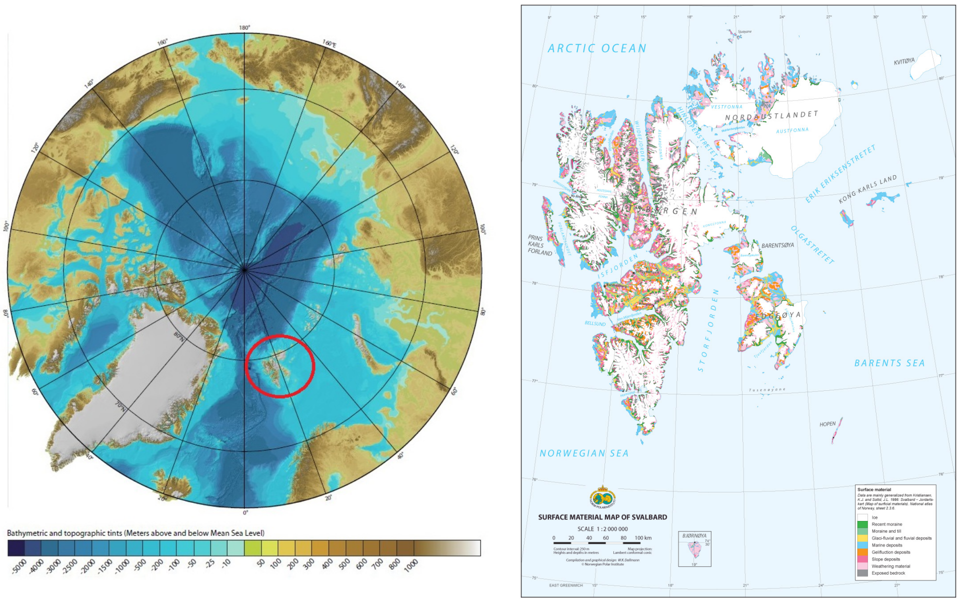

(a)

(b)

Figure 3.1: (a) Svalbards location in the Arctic Ocean, highlighted in a red circle. From The International Bathymetric Chart of the Arctic Ocean (IBCAO) Version 3.0 (Jakobsson et al., 2012). (b) Overview map of Svalbard, showing the surface material. Glaciers and ice caps are indicated by white areas (Norwegian Polar Institute, 2015a).

Figure 3.2: The estimated equlibirum line altitude (ELA) on Svalbard glaciers given as 100 meter contour intervals. Modified from Hagen et al. (2003b) by Ingólfsson (2011).

TABLE 3.1: Average annual and seasonal temperatures and precipitation totals during 1961-1990 and 1981-2010 (adapted from Førland et al. (2011))

Svalbard Airport	1961-1990					1981-2010				
	Annual	Winter	Spring	Summer	Autumn	Annual	Winter	Spring	Summer	Autumn
Temp. [C]	-6.7	-15.1	-10.8	4.2	-5.2	-4.6	-11.7	-8.3	5.2	-3.5
Prec. [mm]	190	52	40	51	49	191	55	31	47	58

Svalbard has one of the longest high-latitude meteorological records on Earth, and the first weather station was established in Grønfjorden in 1911 (Nordli, 2010). Later, the weather station at Svalbard Airport has provided records for both temperature and precipitation. Table 3.1 shows average annual and seasonal temperatures and precipitation totals during 1961-1990 and 1981-2010. In the Standard Normal Period 1961-1990 (WMO 1989) the average annual air temperature at Svalbard Airport was -6.7 °C, whereas in the most recent Normal Period 1981-2010 (WMO 1989) the average annual air temperature increased by 2.1 °C to -4.6 °C. The strongest increase has been in the average winter temperature by 3.4 °C (Førland et al., 2011).

Svalbard is described as a polar desert, which means the precipitation is normally low. In central Spitsbergen precipitation at sea level is about 200 mm per year, while the western coast have about 400 mm of precipitation per year. Higher precipitation is experienced over glaciers due to orographic effects, but they seldom exceed 2-3 meters of snow per year (Hagen et al., 1993). The record from Svalbard Airport in Table 3.1 shows a small decrease in the average spring and summer precipitation compared to the Standard normal period 1961-1990 (WMO1989). In contrast, a small increase for the autumn and winter period can be observed as well. The harsh weather conditions including drifting and blowing snow due to high wind speeds often complicate the precipitation measurements in the Arctic (Førland et al., 2011).

3.1.2 Present glacial and periglacial environment

About 59% (35 528 km^2) of Svalbard is covered by glaciers and ice caps (Nuth et al., 2015). Cirque and valley glaciers are mostly present in the high alpine mountain regions in the western parts of Spitsbergen, and several large ice caps are located in the flatter areas of eastern Spitsbergen, Edgeøya, Barentsøya and Nordaustlandet. There are also some piedmont-type glaciers resting on the strandflats of Prins Karls Forland. Most dominant by area are the Spitsbergen type of glacier: large, continuous glacier complexes divided into individual ice streams by mountain ridges and nunataks, usually terminating in the fjords (Hagen et al., 1993). The majority of the glaciers are polythermal (Hagen and Sætrang, 1991), with parts frozen to the ground in the ablation area and ice at the pressure melting point in the thicker accumulation area. A large number of the smaller cirque glaciers are entirely cold and frozen to the ground, while the warm-based glaciers are probably completely absent due to the presence of continuous permafrost (Hansen, 2003). Due to the cold climate with low temperatures and the small amount of precipitation, the glaciers on Svalbard display low flow rates (Hagen et al., 2003a). Generally, the glaciers ending on land flow much slower compared to calving tidewater glaciers. The fastest glacier on Svalbard is Kronebreen, with a mean annual velocity in the central part of the front of 2 m d^{-1}

(Kääb et al., 2005; Lefauconnier et al., 1994; Melvold, 1992).

The equilibrium line altitude (ELA) distribution over the Svalbard archipelago is a good indicator of the climatic conditions, as temperature and thereby ablation, varies less than precipitation from one region to another. Figure 3.2 modified by Ingólfsson (2011) from Hagen et al. (2003b) shows the pattern of the ELA on Svalbard glaciers, and reflects the precipitation pattern. Most of the precipitation is brought by south-easterly winds and thus lowers the ELA to about 200 m a.s.l in south-eastern Svalbard. In contrast, the ELA is around 800 m a.s.l in the central to northern region. However, it is important to note that the glaciers are not in balance with the existing climate, and that the actual ELA is at present significantly higher than shown in Figure 3.2. The available mass balance measurements are relatively sparse, but all the data measured shows a generally negative trend and no changing trend or increased melting has been observed over the recent decades (Hagen et al., 2003b).

3.2 Borebreen

Borebreen is a tidewater glacier draining into Borebukta, an inlet on the north side of Isfjorden on Spitsbergen (Figure 3.3). The glacier is approximately 22 km long and has a drainage area of 120 km^2 (Hagen et al., 1993). The position of the terminus of the glacier has been mapped for several intervals since its initial observation by De Geer (1910) from oblique and vertical aerial photographs acquired by the Norwegian Polar Institute since the 1930s. The fjord is approximately 1 km wide and 50 m deep at the present glacier front (Ottesen and Dowdeswell, 2006). Based on seafloor mapping in front of Borebreen, Ottesen and Dowdeswell (2006) suggested Borebreen to be a surge-type glacier.

3.3 Tunabreen

Tunabreen is situated almost in the centre of Spitsbergen, east of the largest settlement Longyearbyen. Tunabreen drains from Filchnerfonna and Lomonosovfonna ice caps, and is a 33 km long tidewater glacier calving into the head of Tempelfjorden, the easternmost branch of Isfjorden. It is defined as a surge-type glacier, with surges documented in 1930, 1970 (Hagen et al., 1993) and recently between 2002 and 2005 (Forwick et al., 2010). During its most recent surge in 2002-2005, Tunabreen advanced about 2 km (Flink et al., 2015). It is the only glacier in Svalbard known to have surged three times, producing a consistent return period of approximately 40 years. This rather regular 40-year surge cycle is the shortest known in Svalbard; many of Svalbard's glaciers have surge cycles of over one hundred years (Dowdeswell et al., 1991). Since the last surge termination, Tunabreen has calved back to its present-day position, and is now in its quiescent phase.

Radio echo-sounding records indicate that the glacier is polythermal (Bamber, 1987). The flow regimes of Tunabreen are indicated through structures exposed at the surface of the glacier. Ice stratification and longitudinal foliation are clearly seen

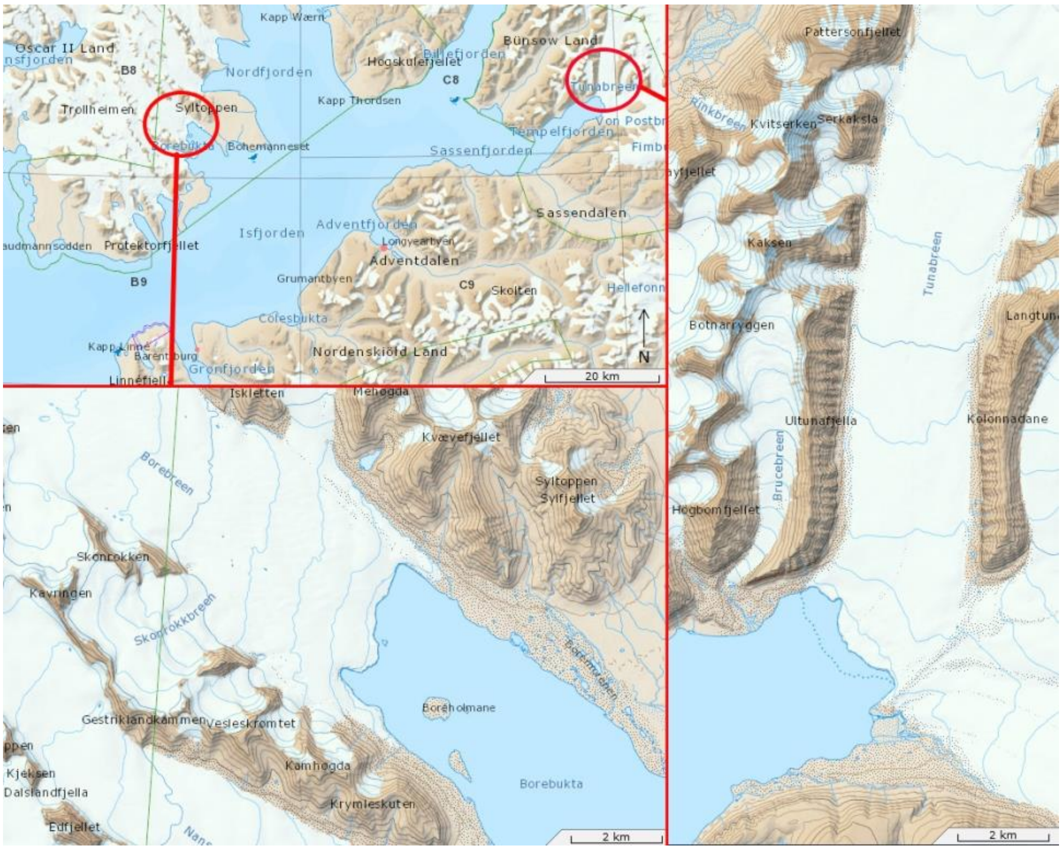

Figure 3.3: Overview map of the location of Borebreen (lower left) and Tunabreen (right) in the Isfjorden area. The location of Austre Torellbreen is shown in Figure 3.5. Basemap from Norwegian Polar Institute (2015b).

in aerial photographs. This stratification, which originates in an orientation defined by the margins of the flow boundaries in the accumulation zone, becomes folded as the ice flows. Fold tightness increases down-glacier, evolving to isoclinal towards the terminus (Fleming et al., 2013). At the height of the most recent surge, the entire length of Tunabreen exhibited intense surface crevassing. The crevasse pattern was dominated by transverse crevasses, formed perpendicular to the longitudinal foliation and glacier flow direction. Mapping of crevasses on Landsat satellite images in Figure 3.4 by Flink et al. (2015) shows up-glacier propagation of crevasses during the surge.

Tunabreen has a mean winter frontal velocity of 0.2 m d^{-1}, and detectional motion during the summer is confined to the frontal zone where high longitudinal stress gradients induce outward stretching of the ice (Luckman et al., in review). Stretching rates are proportional to ice cliff heights, which exhibits systematic seasonal variations in response to calving losses (Flink et al., 2015). The recent study by Luckman et al. (in review), shows a modest advance during the winter and a stronger retreat during the summer, and a net annual retreat of approx. 150 m.

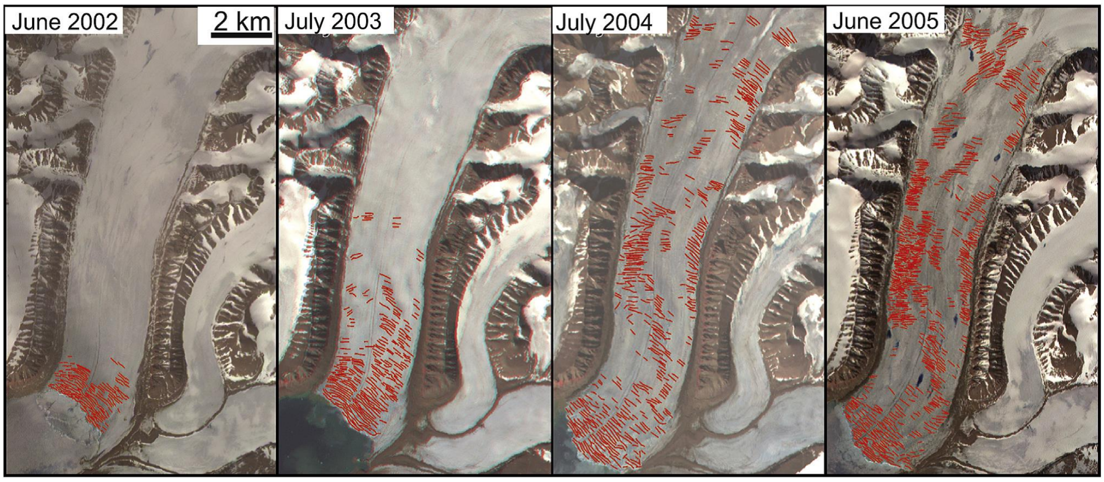

Figure 3.4: Crevasses mapped on Landsat satellite images, showing up-glacier propagation of crevasses during the most recent surge of Tunabreen between 2002 and 2005. From Flink et al. (2015).

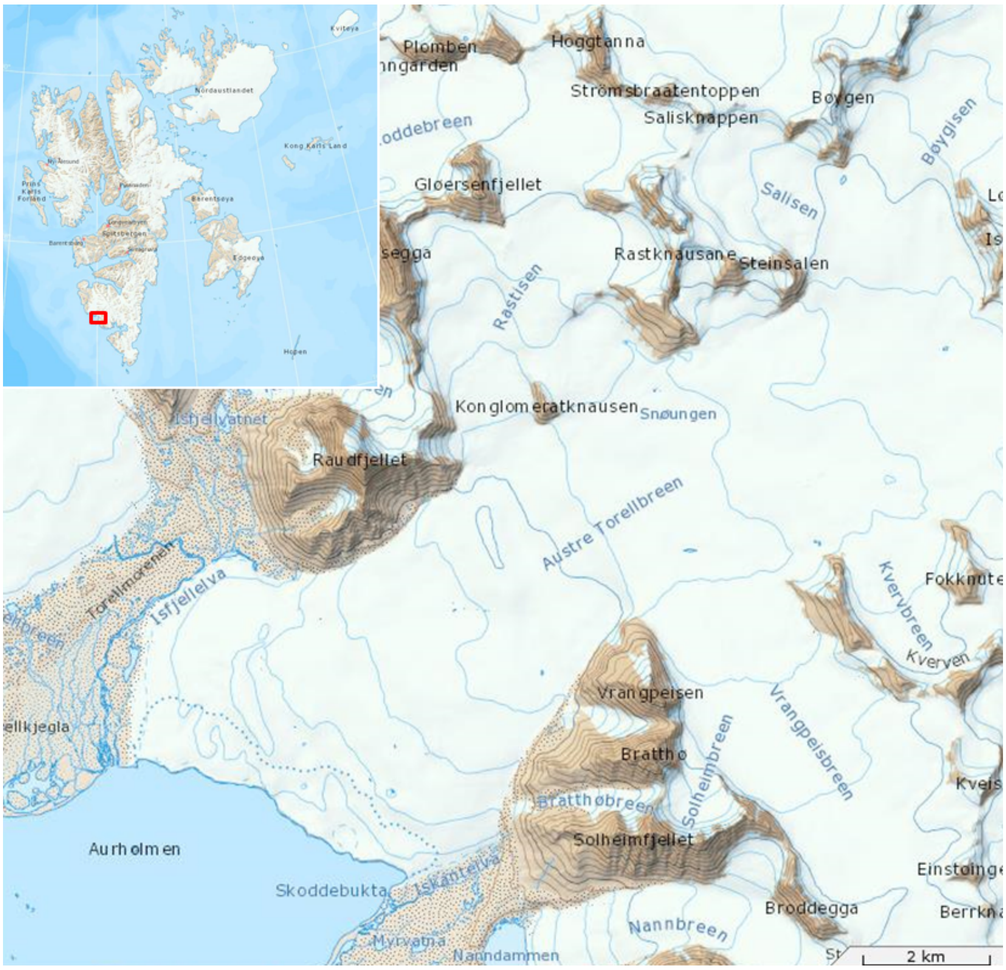

Figure 3.5: The location of Austre Torellbreen along the south western coast of Spitsbergen. Basemap from Norwegian Polar Institute (2015b).

3.4 Austre Torellbreen

Austre Torellbreen is situated along the western coast of Spitsbergen (Figure 3.5) north west of the Polish research station in Hornsund. It is a 136.2 km^2 large tidewater glacier calving into the bay Skoddebukta (Blaszczyk et al., 2009). Austre Torellbreen is draining the accumulation plateau of Amundsenisen to the north east (Hagen et al., 2005). Using GPR data, Navarro Valero et al. (2013) recorded the maximum thickness of Austre Torellbreen to be 619±13 meters. In a study by Blaszczyk et al. (2009), it is defined as a fast-flowing glacier with a calculated velocity of 260 m yr^{-1}. This is measured using feature-tracking techniques on a pair of ASTER images from 2005 and 2006, as seen in Figure 3.6. The estimated calving intensity is calculated to be 0.1056 km^2 yr^{-1}, and the annual retreat from 2005 to 2006 is calculated to be ~75 meters (Blaszczyk et al., 2009).

The crevasse area on Austre Torellbreen extends far up-glacier, in contrast to the terminal crevasse fields on Borebreen and Tunabreen. This may indicate a larger body of fast-flowing ice, with higher velocities extending further away from the front area. Blaszczyk et al. (2009) measured a crevasse zone length of 2000 meters.

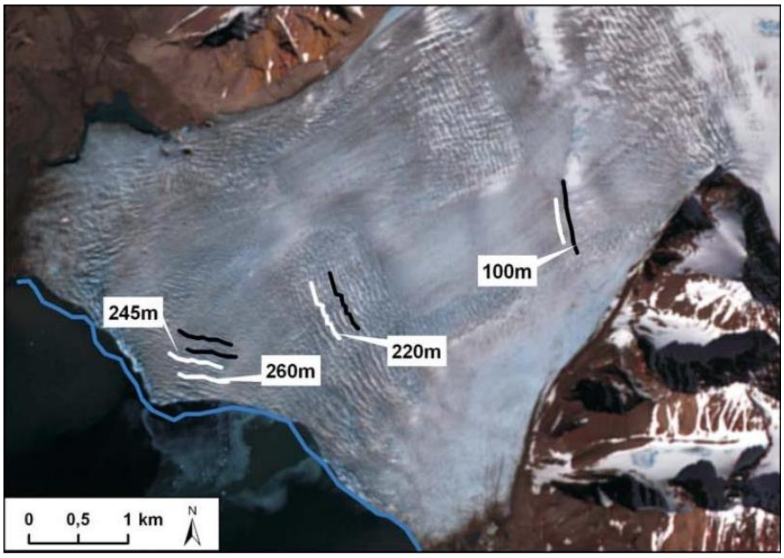

Figure 3.6: Annual flow velocities on the Austre Torellbreen tongue derived from displacement of crevasses on a pair of ASTER images (2005 and 2006). Black lines are the location of crevasses in 2005, white lines are the location of crevasses in 2006 and blue line is the front position in 2005. From Blaszczyk et al. (2009).

CHAPTER 4

DATA AND METHODS

This chapter describes the methods used to collect and process data presented in this thesis. In addition it includes a section defining possible sources of errors and uncertainties that may affect the accuracy and reliability of the data and methods used.

As described in Chapter 1, this project aims to compare TerraSAR-X images with ground truth measurements. Two glaciers in Svalbard were selected, Borebreen and Tunabreen. The crevasses found along the periphery of the terminal crevasse field were mapped and measured in the field (Section 4.1). These data were compared to manual crevasse mapping performed on TSX images acquired within a few days before or after the fieldwork (Section 4.2). The limit of the terminal crevasse field and the glacier front position were mapped on Tunabreen to work out a complete annual cycle of terminal crevasse field migration. This could further be used to investigate the evolution of the crevasse field compared to the velocity and strain rates in this area of the glacier. In addition, the crevasse area of Austre Torellbreen was mapped and compared to a velocity map, to confirm or disprove the results from Tunabreen.

4.1 Crevasse mapping in the field

The fieldwork consisted of measuring crevasse positions and widths on two tidewater glaciers in Svalbard. Borebreen and Tunabreen were chosen as target glaciers for the ground truth measurements. Both are located in the Isfjorden area, and their location, morphology and past dynamics are described in more detail in Section 3.2 and Section 3.3. The lower 1400 and 1700 metres on Borebreen and Tunabreen respectively, present an extensive crevasse field due to calving and longitudinal extension. This represents a very suitable field area for this study. The fieldwork was carried out at the peak of summer to avoid any snow on the glacier surface. Field measurements were focused on the outer margin of the crevasse field because of the accessibility of the glaciers and the safety aspect of the work. In preparation

TABLE 4.1: GPS survey parameters including the settings used on the Leica RX1210 unit.

GPS survey parameters	
Rover unit	Leica RX1210
Antenna	Leica ATX1230
Antenna height	1.0 m
Coordinate system	WGS84
Coordinate type	Geodetic
Cut-off angle	13°
GNSS type	GPS
Logging type	Static and moving
Logging rate	1.0 s (both for rover and base station)

to fieldwork, a TerraSAR-X image of each glacier was mapped in ArcMap. The mapped crevasses were exported as tracks and transferred to a hand held Garmin GPS unit. This was done so that the area where there was no crevasses visible on the TerraSAR-X images could be investigated closer in the field.

The fieldwork was carried out on Borebreen July 18th 2014 and on Tunabreen August 1st 2014. Borebreen was accessed on the north east side of the glacier, and the measurements were done by walking across the glacier in a distance of approximately 3700 m about 1300 m up-glacier from the front. The observed crevasses in this area of the glacier were quite small and with some space in between, which made it possible to cover a large area of crevasse measurements. Tunabreen was accessed on the south west side, passing some of the remaining surge moraines. The glacier was heavily crevassed in the front, and had to be entered about 1600 m up-glacier from the front. The transverse crevasses in this area were elongated and wide, and some of them were impossible to cross without more advanced safety equipment. This made it hard to cover a large area with mapping, hence the mapping on Tunabreen was mainly done in the upper part of the crevasse field on the south west edge of the glacier.

Global Positioning System (GPS) was used to measure the position of crevasses on the surface of the glacier. GPS relies on a constellation of satellites that constantly broadcast a time signal. This signal is received using an antenna and a rover unit. The time for a signal to be sent and received is measured to allow the ground receiver to calculate its own position. For enhanced accuracy, a base station is used to measure the position of the satellites to work out how much difference there is between their predicted and actual positions. This information is used to correct the position data collected by the rover, in this case by post-processing the data. Base station data was provided by Kartverket from the base station in Longyearbyen (78°13’43.77230” N, 15°23’50.31623” E, WGS84).

The equipment used for doing the GPS measurements on the selected glaciers was a Leica RX1210 unit and a Leica ATX1230 antenna (Figure 4.1) mounted on a 1 m pole.

The GPS survey settings are presented in Table 4.1. The start, middle and end point of each crevasse was recorded, in addition to a width measurement at each point. For every point measured, the GPS antenna was set to log for at least 10 seconds at the specific point on the glacier surface (Figure 4.2). This was to make sure that each point was occupied for a minimum time of double both the logging rate (1.0 s) and the interval rate of the base station data (1.0 s). Every position measurement was saved on the Leica rover with an individual point ID.

Crevasse width measurements were done using a measuring tape. The crevasse width was measured at the same point as the recorded position. The width measurements are done to the nearest 5 cm. Some of the crevasses were too wide to cross, making it impossible to get an accurate width measurement. These crevasses are referred to as >150 cm wide, and this is commented on in Table 5.1 and Table 5.2 for Tunabreen and Borebreen respectively. Measurements were conducted in the same way on both glaciers.

When processing the crevasse width data, each crevasse is assigned with the maximum crevasse width measured on the specific crevasse. This width is used to classify the crevasse into one of four different classes: <50 cm (class 1), 50-100 cm (class 2), 101-150 cm (class 3) and >150 cm (class 4). The crevasse position on the crevasse map includes all the recorded positions and the maximum crevasse width for each crevasse. This means that the crevasse may not be as large as the given size at the specific position, but the given size reflects the maximum size of the crevasse.

Figure 4.1: A Leica RX1250 (right) mounted with a Leica ATX1230 antenna (left) was used for positioning on the glacier. Photo: Leica Geosystems.

The raw survey data and the base station data were imported to the Leica Geo Office software version 4.0 (Leica Geosystems AG). The processing parameters were configured according to the survey parameters (Table 4.1), and the processing intervals were selected. This includes both the rover intervals and the base station intervals from the time the survey started until the final measurement. The Leica Geo Office software automatically processes the selected data, and the output gives the

Figure 4.2: Measuring the end point of a crevasse on Tunabreen. Photo: Doug Benn, 2014.

corrected GPS positions with a more accurate position compared to raw GPS data. A study of differential GPS (DGPS) accuracy in Portugal by Monteiro et al. (2005) suggests a degradation of 0.22 m per 100 km. The distance from the base station in Longyearbyen to Borebreen and Tunabreen is 40 km and 50 km, respectively. The output from the post processing in Leica Geo Office was in latitude-longitude coordinates, and was converted to UTM coordinates. The coordinates could then easily be imported to the UTM zone 33 north coordinate system used by ArcMap. Results of crevasse mapping in the field is presented in Section 5.1.

4.2 Crevasse mapping with SAR images in ArcMap

The mapping of the crevasse fields was carried out using TerraSAR-X (TSX) satellite radar images. The advantage of using radar images compared to optical images is the fact that microwaves are independent on weather conditions and the availability of daylight. The latter is a large advantage for the location of Svalbard, where there is almost five months of polar night during the year. In addition, the TSX satellite has a near-polar orbit resulting in a good coverage of the polar areas. The images selected in this study are provided and processed by professor Adrian Luckman (Swansea University/UNIS). They are all co-registered to the first image in the sequence to less than a pixel, and orthorectified using a digital elevation model (DEM). In addition, an intensity image is created from the single-look-complex data. They are also decibel scaled and converted to geotiffs (Luckman, personal communication, 2015).

The images used for this study are the TSX stripmap mode images. The stripmap mode (SM) is the basic imaging mode with a resolution up to 2-3 meters. Parameters for the TSX satellite and the specific stripmap mode images are listed in Table

TABLE 4.2: Parameters for the TerraSAR-X satellite and for the stripmap mode (SM) images used in this study. From German Aerospace Center (DLR).

Orbit and attitude parameters	
Orbit height	514 km
Revistit time (orbit prepeat cycle)	11 days
Inclination	97.44°
Radar frequency	9.65 Gigahertz

Stripmap mode parameters	
Swath width	31.588 km
Minimum incidence angle	31.756°
Maximum incidence angle	34.564°
Number of elevation beams	27
Ground range resolution	1.70 m to 3.49 m (at 45° to 20° incidence angle)

4.2. It was not known in advance if the crevasse mapping would be possible to do based on the TSX images, because of the 2-3 meters resolution given by the German Aero Space Centre (DLR). Some crevasses are smaller than the sample spacing of the stripmap images. The images come in cycles of 11 days, but the images used are from every 22 days (every second image in the cycle is used). The reason for mapping every second image in the 11-days cycle is limited available time to carry out the manually mapping. By mapping the images in a 22-days cycle, a longer time period could be covered. The images used in the crevasse area limit and front line mapping of Tunabreen described in Section 4.2.1 are from February 9th 2013 to April 1st 2015. The images used for the crevasse maps based on field measurements from Borebreen and Tunabreen are from August 23rd 2014 and July 11th 2014, respectively. The image used for the mapping of the crevasse field on Austre Torellbreen is from February 13th 2013.

The mapping of crevasse features on the TSX images was done manually, and no automatic classification method was used. As illustrated in Figure 5.3a and Figure 5.4a in Chapter 5, it is easy to discriminate between crevassed and non-crevassed areas on the glacier surface. Zones with crevasses appear as a succession of shadows and bright lines. The darkness or brightness is decided by the backscatter from the glacier surface, depending on the snow cover, water content and temperature conditions. Dry snow and rough ice will give bright backscatter values, while wet snow and ice will give dark backscatter values. The backscatter will be different from image to image because of the change in conditions during the 11-day period. This is why it is hard to use automatic classification methods for the crevasse mapping. The manual mapping of crevasses on the TSX images is based on linear features in combination with backscatter changes. The mapping was focused on the terminal crevasse field. Meltwater channels were avoided by focusing on the transverse lines in the images.

The TerraSAR-X images were imported to ArcMap version 10.1 (Esri 2012), and projected into the WGS84 UTM zone 33 north (Figure 4.3). A shapefile was created with the same projection, and crevasses were marked manually using the editor-tool to draw blue polylines along the crevasses on the glacier (Figure 4.4). In addition, the measured coordinates from the field survey were added as attribute points on the crevasse map (Figure 4.5). The points were given four different colors depending on their assigned class of maximum crevasse width measured in field; <50 cm (class 1), 50-100 cm (class 2), 101-150 cm (class 3) and >150 cm (class 4) (Figure 4.6). Results of the crevasse mapping and corresponding field measurements are presented in Section 5.1.

4.2.1 Crevasse area limit and front line mapping

Mapping the terminal crevasse field of tidewater glaciers enable a further investigation of glacier dynamics and how the development of crevasses are linked to strain rates and glacier velocity. In addition to try to assess the method of using TSX images to map crevasses on glaciers, another important aim of this thesis is to investigate the relationship between the glacier front position and the crevasse area limit in a complete annual cycle. To do this a total of 32 TSX images of Tunabreen were used. The extent of the terminal crevasse field on each image was delineated as well as defining the glacier front position. The limit of the crevasse area was marked in a new shapefile, using a red polyline drawn from the glacier front around all the marked crevasses ending up at the glacier front in an u-shape. This limit is defined by the end point of the outer crevasses marked in the crevasse area (Figure 4.7). The glacier front position was marked in a separate shapefile as a green polyline (Figure 4.7). Both the crevasse area limit line and the front position line were converted to XY coordinates (WGS84, UTM zone 33 north) using the data management tool in ArcMap. The XY coordinates correspond to the exact line, not only the beginning and the end of the polylines. The XY coordinates were exported as two separate text files for each image; one for the glacier front position line and one for the crevasse area limit line (Figure 4.8). Two of the mapped images are presented and described more in detail in Section 5.2. To visualize the results from the crevasse area limit line and glacier front line mapping, the XY coordinates of both the crevasse area limit line and the front line were plotted in a UTM plot using MATLAB version 2010a (Mathworks). This resulted in a UTM plot presented in Section 5.2.

A transect line was drawn in order to plot a time/distance diagram of the front position and crevasse area limit variations. The line was drawn as a straight line from a point in the fjord in front of the glacier to a point on the glacier surface behind the crevasse area limit. The transect line was drawn perpendicular to the crevasse orientations in the area of the glacier where the velocities are the highest throughout the year, defined from the velocity maps presented in Figure 5.9. The distances from the start point of the line to the glacier front and from the start point to the crevasse area limit line are measured in each image in ArcMap using the measuring tool. The distance measurements are plotted in a time/distance diagram using MATLAB version 2010a (Mathworks). The time/distance diagram is presented in Section 5.2.

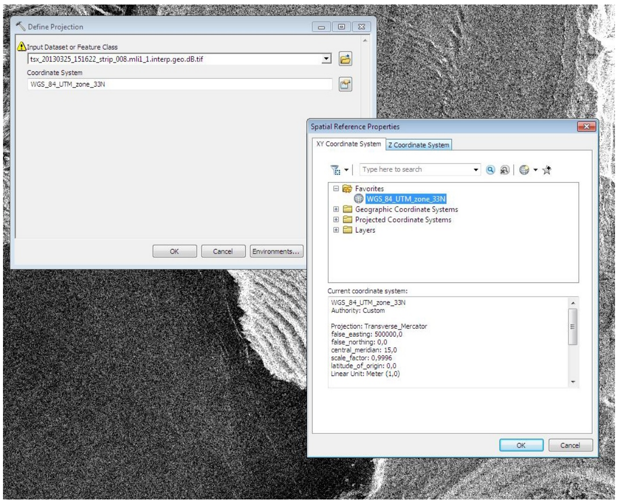

Input Dataset or Feature Class: tsx_20130325_151622_strip_008.mli1_1.interp.geo.dB.tif

Coordinate System: WGS_84_UTM_zone_33N

Current coordinate system:

WGS_84_UTM_zone_33N
Authority: Custom

Projection: Transverse_Mercator
false_easting: 500000,0
false_northing: 0,0
central_meridian: 15,0
scale_factor: 0,9996
latitude_of_origin: 0,0
Linear Unit: Meter (1,0)

Figure 4.3: Defining projection of the TerraSAR-X image in ArcMap. The projection used is the WGS84 UTM zone 33 north.

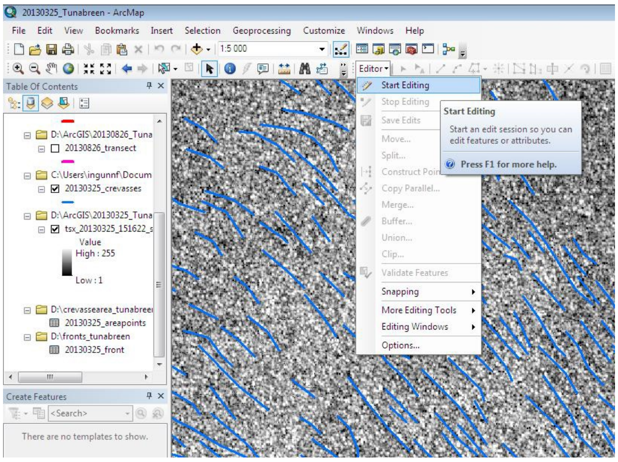

There are no templates to show.

Start an edit session so you can edit features or attributes.

Press F1 for more help.

Figure 4.4: Activating the editor tool in ArcMap, which was used to mark all crevasses as blue polylines.

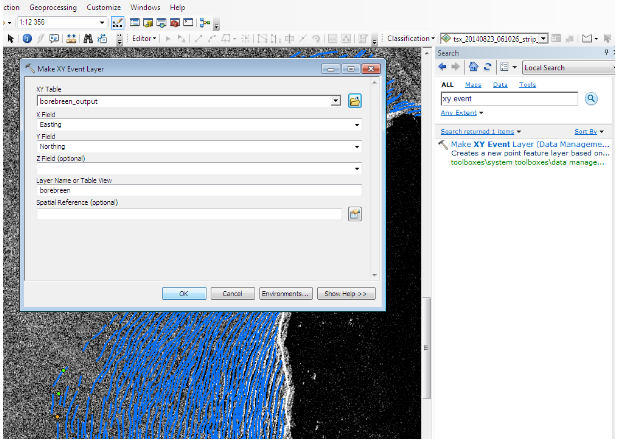

XY Table: borebreen_output

X Field: Easting

Y Field: Northing

Z Field (optional):

Layer Name or Table View: borebreen

Spatial Reference (optional):

Search: xy event

Make **XY Event** Layer (Data Manageme...
Creates a new point feature layer based on...
toolboxes\system toolboxes\data manage...

Figure 4.5: Importing the UTM coordinates (WGS84) from the field measurements as attribute points in the crevasse map.

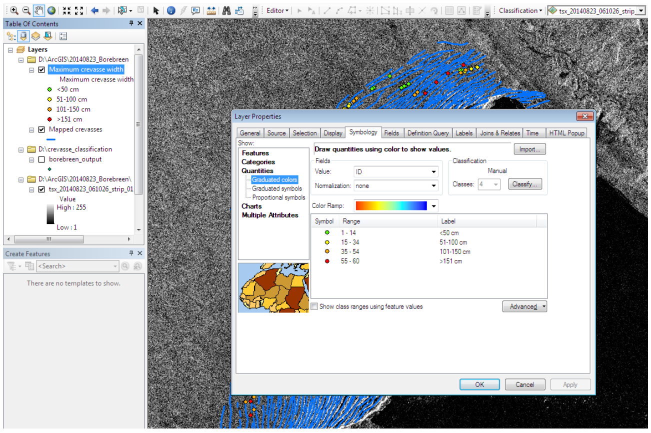

Layer Properties

Symbology

Draw quantities using color to show values.

Fields

Value: ID

Normalization: none

Classification

Manual

Classes: 4

Symbol	Range	Label
🟢	1 - 14	<50 cm
🟡	15 - 34	51-100 cm
🟠	35 - 54	101-150 cm
🔴	55 - 60	>151 cm

☐ Show class ranges using feature values

Figure 4.6: Assigning the imported attribute points to the four different classes, giving them individual colours for each class.

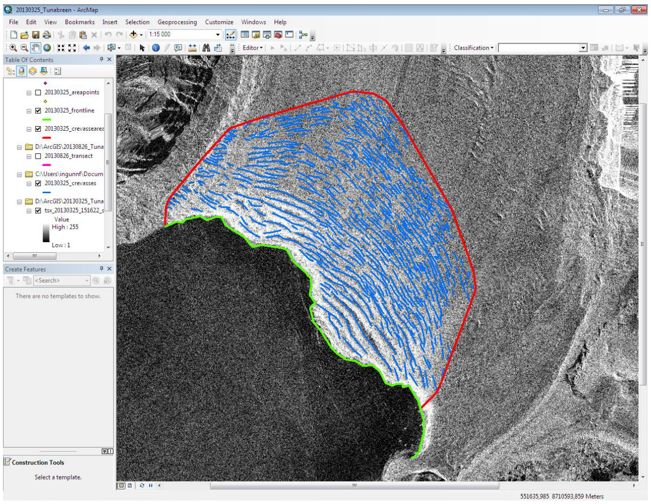

Figure 4.7: TerraSAR-X image displayed in ArcMap, showing polylines defining the individual crevasses (blue lines), the crevasse area limit (red line) and the glacier front position (green line).

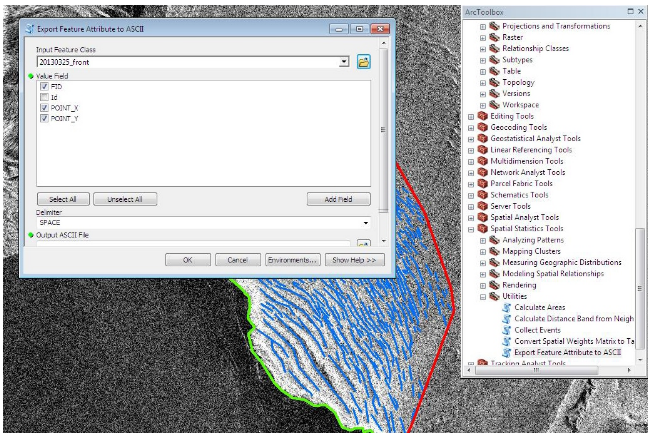

Export Feature Attribute to ASCII

Input Feature Class

20130325_front

Value Field

☑ FID

☐ Id

☑ POINT_X

☑ POINT_Y

Delimiter

SPACE

Output ASCII File

Figure 4.8: Exporting the XY coordinates of the crevasse area limit line and the glacier front position line as text files.

To compare the results from the mapping of the crevasse field on Tunabreen, one TSX image from Austre Torellbreen was also mapped in ArcMap. This included mapping of crevasses, crevasse area limit line and front line as previously described. The results of this mapping is presented in Section 5.3.

4.2.2 Velocity and strain rate maps

In addition to investigating the relationship between the terminal crevasse area limit and the front line positions, velocity and strain rate maps have been compared to the mapped terminal crevasse field on Tunabreen. The strain rate and velocity maps are based on feature tracking from two TSX images in a 11-day cycle, provided by professor Adrian Luckman (Swansea University/UNIS) in spring 2015. The summer TSX images are too noisy for feature tracking. For this reason winter TSX images have been chosen to calculate the 1st principal strain rate and velocity of the front area on Tunabreen (Luckman, personal communication 2015).

The strain rate maps and velocity maps used in this study are from three different 11-day cycles: February 9th to 20th 2013, October 10th to 20th 2013 and December 3rd to 14th 2013. The 1st principal strain rates along a transect from the glacier front to the crevasse area limit line is extracted and presented in one strain rate plot for each strain rate map. The transect line used for this is the same transect line used in the UTM plot and the time/distance diagram as described in the previous subsection. The strain maps were imported into ArcMap and georeferenced to WGS84 UTM zone 33 north. The transect line was added as a shapefile. Every pixel along the transect line containing a calculated strain rate value (given as a color) was marked as a point. The extracted strain rate value and the corresponding distance from the glacier front line to the specific point along the transect were noted in a text file. The strain rate at each specific point along the transect was plotted in a strain rate plot using MATLAB (Mathworks, 2010a). The same procedure was performed to the velocity maps as well. The plots of strain rates and velocities along the transect line from the glacier front to the crevasse area limit line are presented in Section 5.3.

The calculated velocities on Tunabreen are limited to the glacier front area. The calculated strain rates extend in an area further up-glacier, and covers large parts of the mapped crevasse field. Based on this, strain rates along the crevasse area limit line were extracted and added as square points along the line in ArcMap. The strain rate maps showing the calculated strain rate along the crevasse area limit line are presented in Section 5.3.

A velocity map is also compared to the mapped crevasse field on Austre Torellbreen. As for Tunabreen, this velocity map was provided by professor Adrian Luckman (Swansea University/UNIS) in spring 2015. The velocity map is based on feature tracking from two TSX images in a 11-day cycle from February 13th to 24th 2013, and is presented in Section 5.3.

4.3 Errors and uncertainties

4.3.1 GPS measurements

Errors in calculating GPS position can come from a number of sources, including atmospheric interference, topographic shading, low satellite azimuths, long baseline and human error in instrument settings and physical placement. The cut-off angle for satellite azimuth was set to 13° to avoid excessive atmospheric interference affecting precision of received signals. This may have reduced the number of satellites, but there were still a adequate number of satellites at any one time when taking positions in the field. The baselines between the base station in Longyearbyen and the field sites were 40 km and 50 km, for Borebreen and Tunabreen respectively. The study by Monteiro et al. (2005) suggests a degradation of 0.22 m per 100 km away from base station. This will give a degradation of 0.088 m for the field site on Borebreen and 0.11 m for the field site on Tunabreen. The quality of positions calculated by the manufacturer (Leica Geosystems) is given as a horizontal accuracy of 5 mm + 0.5 ppm for static surveys like the one performed in this study. This accuracy is likely to be extremely optimistic given all the listed sources of errors. Given that the degradation is 0.088 m and 0.11 m for the two field sites, it is more reasonable to work with an estimated error of ±0.1 m for all positions recorded in this study.

4.3.2 Mapping of TerraSAR-X images

As described in section 4.2, the TSX images used are geotiffs which are co-registered to about a fraction of a pixel. This means that the image-to-image geometric consistency is good, but the lack of a good quality DEM from both Borebreen and Tunabreen areas leads to a less accurate correspondence to ground coordinates. Based on this, there will be a deviation between the measured coordinates of the crevasses on the glacier surface and the coordinates of the crevasses recognized on the TSX image. This deviation is not known, and will vary from one point to another. This means that the position of the crevasse measured in the field will probably not perfectly match the position of the crevasses mapped on the TSX images. To improve this, a better DEM for the area is required.

The accuracy of the manually mapping of crevasses on the TSX images may be affected by the temperature and surface conditions on the glacier. Where the surface temperature goes above the melting point, and especially when there is snow around, the backscatter drops very quickly. This will give a dark or black image, which in turn leads to difficulties to interpret crevasses in the summer months. Where snow fills or covers the crevasses, it may be transparent to the radar if it is very cold. This will give bright or white images where crevasses are hard to separate from the surrounding glacier surface. The very dark or very bright images seem to blur the smallest crevasses which are found in the outer parts of the terminal crevasse fields. When defining the crevasse area limit, this will give a smaller crevasse area with a limit line closer to the front line, which can be seen on some of the summer and winter images (examples presented in Section 5.2).

The strong white reflector near the front position of the glacier observed on some of the images, is not defining the actual front position. This reflector is probably a result of different surfaces connected to the ice cliffs at the ice front and the water in front of the glacier. The glacier front position is defined as the limit where the dark area (water) meets the more scattered bright area (glacier ice and snow). This limit is quite clear and can easily be identified on all the mapped images.

The lines of high strain in the winter strain maps are associated with the discontinuity problem in the feature tracking algorithm. This happens when the displacement jumps between integer numbers of pixels. It is possible to improve this with extra processing, but this is not done for the strain maps used in this study due to time constraints.

CHAPTER 5

RESULTS

The following chapter presents the results from the field measurements and the manual crevasse mapping of the TerraSAR-X images in ArcMap. Strain rate maps and velocity maps from Tunabreen are presented and compared to the data from the crevasse mapping. In addition, a crevasse map and a velocity map from Austre Torellbreen are presented.

5.1 Ground truth measurements

The following section describes the results of the ground truth measurements from the fieldwork done on Tunabreen and Borebreen. The position measurements and the maximum width of each crevasse are presented in Table 5.1 and Table 5.2 for Tunabreen and Borebreen respectively. Included in the tables are the classifications of each crevasse measured as described in Section 4.1. In addition, crevasse maps of Tunabreen and Borebreen are presented in Figure 5.1 and Figure 5.2. The figures are based on the positions and maximum width measurements of the crevasses done on both glaciers, as well as the crevasses mapped in ArcMap. The mapped crevasses in ArcMap appear as blue lines, and the field measurements are presented as circle points with different colours depending on their assigned width class. The classes and corresponding colours are presented in the legends on the maps. Position and width measurements of the crevasses are taken at two or more points. During post processing of the data, the maximum width measurement was assigned to all the positions of the crevasse as described in Section 4.1. This gives two or more points in the crevasse map showing the position and maximum width of each crevasse.

The crevasse survey data from Tunabreen in Table 5.1 shows the distribution of the maximum width measurements based on the four defined classes as described in Section 4.1. The crevasse map of Tunabreen seen in Figure 5.1 shows the limited area where the ground measurements were possible to conduct during the day of fieldwork. The area is restricted to the upper western part of the crevasse area. The

TABLE 5.1: Table presenting the results of the crevasse survey done at Tunabreen Friday August 1st 2014. Each crevasse is given a maximum width in centimeters, which is the largest width measured at any point of the crevasse. The maximum width defines its assigned class. Every measured position is specified as a start, middle or end point of a crevasse. The position measurements are given in UTM coordinates (WGS84, UTM zone 33 north). Where the crevasse is too wide to cross to get an accurate width measurement or merges with other crevasses, this is commented as "Wide" or "Merge", respectively.

Tunabreen crevasse survey (Friday August 1st 2014)

Crevasse no.	Max width [cm]	Class	Point no.	Description	Easting	Northing	Comments
1	100	2	1	Start	552782.425	8711229.778	
			2	Middle	552840.043	8711257.367	
			3	End	552868.961	8711271.084	
2	55	2	4	Start	552870.218	8711295.025	
			5	End	552903.075	8711306.779	
3	55	2	6	Start	552911.714	8711308.699	
			7	End	552934.879	8711317.933	
4	50	2	8	Start	552955.149	8711321.895	
			9	End	552963.433	8711326.548	
5	40	1	10	Start	552961.370	8711326.484	
			11	End	552963.393	8711328.392	
6	100	2	12	Start	552963.186	8711327.923	
			13	End	552984.971	8711336.797	
7	60	2	14	Start	552980.284	8711333.926	
			15	End	553001.628	8711343.914	
8	65	2	16	Start	552998.393	8711342.654	
			17	End	553021.041	8711353.621	
9	40	1	18	Start	553032.138	8711374.229	
			19	End	553047.449	8711379.216	
10	80	2	20	Start	553045.707	8711375.797	
			21	End	553071.424	8711386.763	
11	65	2	22	Start	553070.828	8711384.192	
			23	End	553087.526	8711391.864	
12	>150	4	24	Start	553172.833	8711372.680	Wide
			25	End	553078.354	8711347.413	Wide
13	>150	4	26	Start	553081.500	8711348.277	Wide
			27	End	553024.737	8711326.815	Wide
14	>150	4	28	Start	553023.761	8711249.346	Wide
			29	End	552979.115	8711228.182	Merge
15	70	2	29	Start	552979.115	8711228.182	Merge
			30	End	552922.795	8711205.285	
16	65	2	31	Start	552926.467	8711206.495	
			32	End	552895.920	8711194.588	
17	120	3	33	Start	552918.099	8711155.117	
			34	End	552879.913	8711141.858	
18	110	3	35	Start	552882.360	8711142.738	
			36	End	552856.969	8711131.161	
19	140	3	37	Start	552859.324	8711068.092	
			38	End	552834.287	8711058.273	
20	>150	4	39	Middle	552839.595	8711043.103	Wide

TABLE 5.2: Crevasse survey at Borebreen Friday July 18th 2014. See table 5.1 for detailed caption.

Borebreen crevasse survey (Friday July 18th 2014)

Crevasse no.	Max width [cm]	Class	Point no.	Description	Easting	Northing	Comments
1	75	2	1	Start	479261.293	8706874.293	Merge
			2	Start	479262.622	8706869.697	Merge
			3	End	479222.678	8706853.007	
2	75	2	4	Start	479221.986	8706858.779	
			5	End	479176.348	8706837.057	
3	110	3	6	Start	479179.998	8706847.447	
			7	End	479144.900	8706831.070	
4	50	2	8	Start	479151.967	8706850.495	Merge
			9	End	479140.663	8706844.178	
5	370	4	10	Start	479165.449	8706886.808	
			11	Middle	479052.470	8706825.696	
			12	Middle	478971.982	8706763.661	
			13	End	478891.346	8706681.377	
6	120	3	14	Start	478834.867	8706690.011	
			15	End	478814.893	8706669.342	
7	20	1	16	Start	478772.605	8706749.018	
			17	End	478747.931	8706733.145	
8	30	1	18	Start	478741.085	8706733.310	
			19	End	478721.293	8706722.488	
9	40	1	20	Start	478636.137	8706805.534	
			21	Middle	478521.685	8706723.815	
			22	End	478510.035	8706715.125	
10	140	3	23	Start	478400.355	8706645.340	
			24	End	478377.559	8706627.517	
11	100	2	24	Start	478377.559	8706627.517	
			25	End	478345.808	8706603.669	
12	80	2	26	Start	478343.766	8706592.275	
			27	Middle	478316.260	8706570.164	
			28	End	478305.222	8706560.711	
13	60	2	29	Start	478308.387	8706566.473	
			30	End	478257.683	8706528.251	
14	85	2	31	Start	478235.579	8706485.681	
			32	End	478164.817	8706413.615	
15	55	2	33	Start	478160.544	8706398.516	
			34	End	478053.861	8706287.599	
16	20	1	35	Start	477873.733	8706081.737	
			36	Middle	477830.076	8706024.565	
			37	End	477781.673	8705967.131	
17	20	1	40	Start	477619.411	8705279.324	
			41	End	477592.902	8705154.686	
18	130	3	41	Start	477592.902	8705154.686	
			42	End	477587.150	8705031.640	
19	140	3	44	Start	477569.156	8704869.937	
			45	End	477571.332	8704803.044	
20	90	2	46	Start	477569.211	8704808.316	
			47	End	477571.757	8704781.084	
21	120	3	48	Start	477574.031	8704782.363	
			49	End	477600.117	8704604.423	
22	125	3	50	Start	477594.062	8704561.173	
			51	End	477604.379	8704471.212	
23	200	4	52	Start	477642.656	8704378.464	Merge
			53	End	477641.662	8704477.377	
24	140	3	54	Start	477666.739	8704417.172	
			55	End	477662.739	8704506.959	
25	135	3	56	Start	477663.411	8704509.687	
			57	End	477659.980	8704558.323	
26	110	3	58	Middle	477672.553	8704643.168	
			59	End	477650.457	8704889.039	
27	60	2	60	Start	477995.925	8705744.407	
			61	End	478047.986	8705822.230	

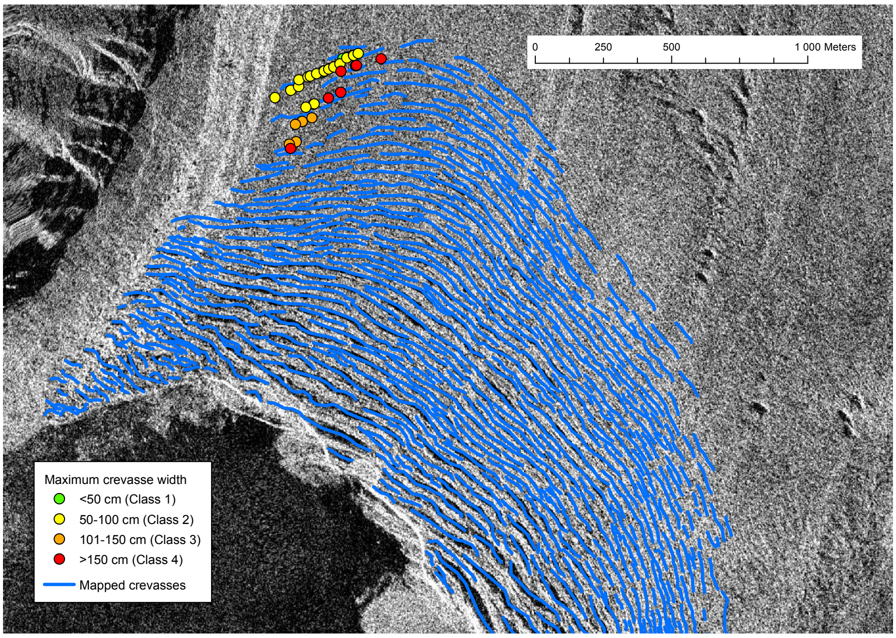

Figure 5.1: Crevasse map of Tunabreen based on a TerraSAR-X image dated July 11th 2014. The mapped crevasses are marked as blue lines, and the maximum widths for each crevasse measured in field is indicated by coloured points defined by four different classes as described in the legend.

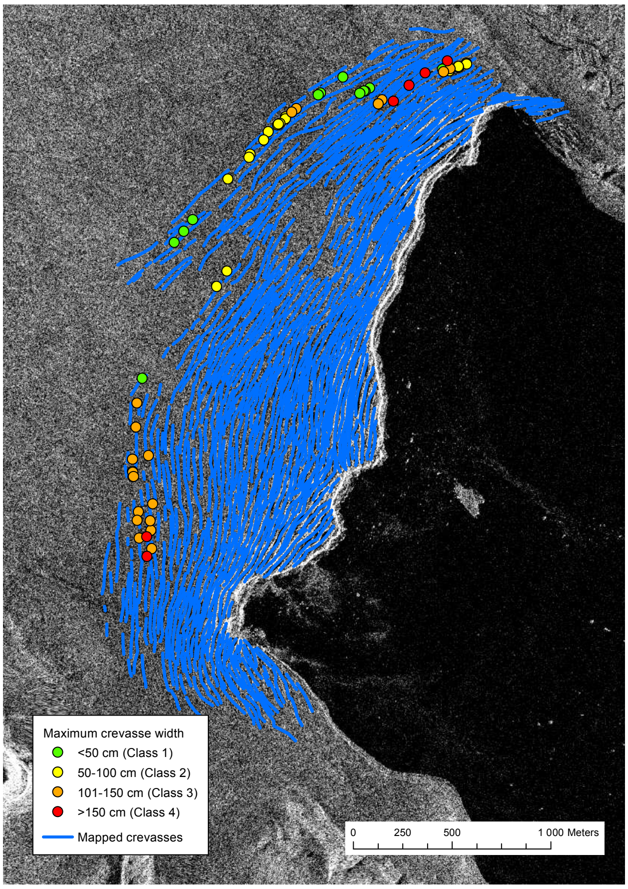

Figure 5.2: Crevasse map of Borebreen based on a TerraSAR-X image dated August 23rd 2014. See Figure 5.1 for detailed caption.

widest crevasses (>150 cm, red points) are mainly located in the inner/lower part of the investigated area, and the narrower ones (<50 cm, green points) are located in the upper, outer part of the mapped crevasse area. As seen on the crevasse map in Figure 5.1 and in Table 5.1, the majority of the measured crevasses on Tunabreen have a width between 51-100 cm (class 2). All the crevasses measured are located within the mapped crevasse field.

The crevasse survey data from Borebreen in Table 5.2 shows the distribution of the maximum width measurements based on the defined classes described in Section 4.1. The crevasse map of Borebreen in Figure 5.2 shows the distribution of the measured crevasses. The two largest measured crevasses (>150 cm, red points) are located in the lower part of the investigated area; one in the southwestern part and one in the northeastern part. The other measurements are more scattered in the upper part of the mapped area but with two large clusters closer to the edges of the glacier. The central area of the glacier has parts with no mapped or measured crevasses at all. The narrowest measured crevasses (<50 cm, green points) are found in the upper part of the crevasse area. Some of the narrowest crevasses in class 1 and 2 (green and yellow points) can not be related to specific mapped crevasses on the TSX image. All the crevasses measured in the field are located within the mapped crevasse field.

5.2 Crevasse limit and front position mapping

The manual mapping of TerraSAR-X images in ArcMap resulted in 32 crevasse maps of Tunabreen in a 22-days cycle from February 9th 2013 to April 1st 2015. Two examples of the terminal field crevasse limit maps are presented in pairs with the raw TSX image in Figure 5.3 and Figure 5.4. These figures show the difference in summer and winter images in terms of backscatter. The raw TSX image from May 5th 2013 in Figure 5.3a is very dark because of low backscatter. This happens when a lot of the microwaves are absorbed by the glacier surface, which in this case may be covered by wet snow or ice. The low backscatter makes it hard to identify features like crevasses, and the mapped terminal crevasse field line in Figure 5.3b may not represent the actual crevasse limit. The raw TSX image from January 1st 2014 in Figure 5.4a is bright and contains more details compared to the summer image. This is because of high backscatter due to dry conditions on the glacier surface, and the crevasses are easily identified in a larger area up-glacier from the front. The mapped terminal crevasse field line on the winter image in Figure 5.4b is more extensive compared to the mapped crevasse area limit line on the summer image in Figure 5.3b.

The crevasse field limit line and glacier front position from all the 32 mapped TSX images, as well as the transect line, is plotted in the UTM plot in Figure 5.5. The corresponding crevasse field limit line and front position from the same date is presented in equal colours. The dates and the associated colours are presented in the legend. The general trend during the entire period from midwinter 2013 towards spring 2015 is a retreating glacier front and a crevasse field propagating up-glacier. There are two clear periods of front line retreat, one from June to October in 2013, and an even more distinct one from July to October in 2014. The crevasse field limit

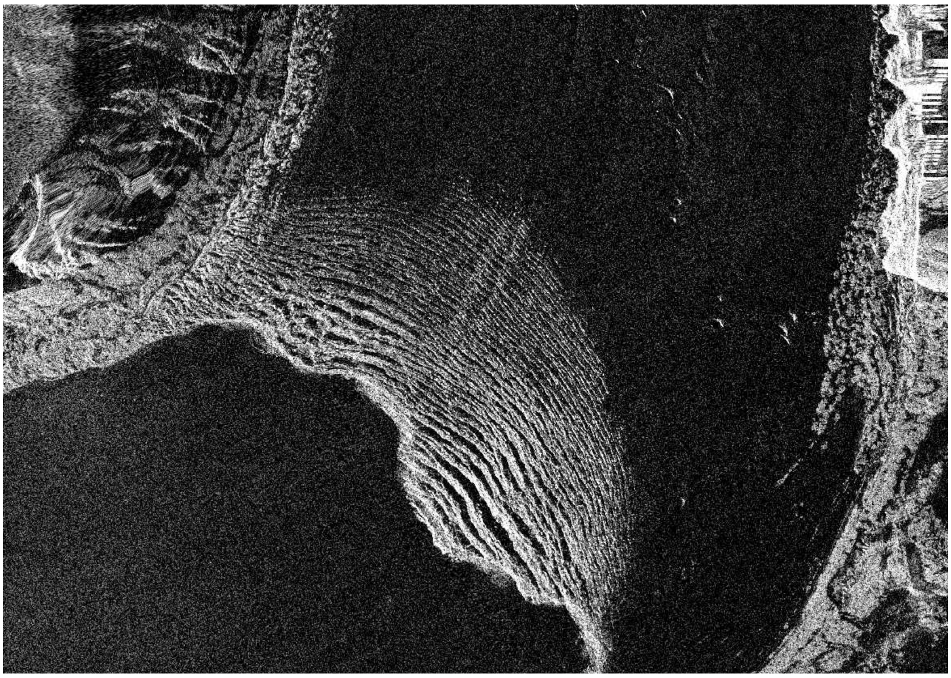

(a) Original TSX image.

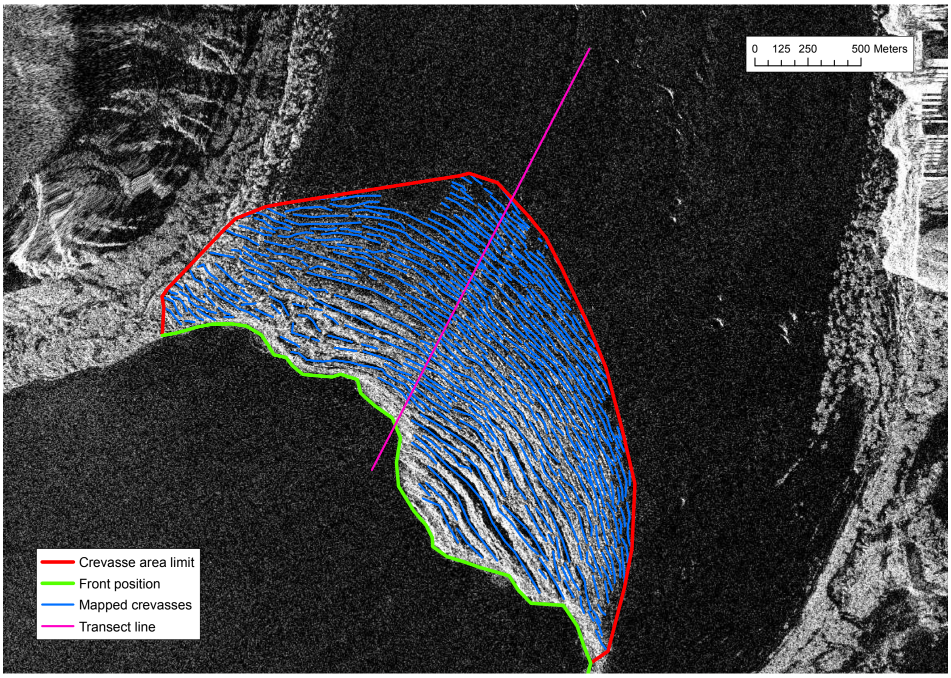

(b) TSX image including mapped crevasses, crevasse limit line, front position and transect line.

Figure 5.3: Raw TSX image (a) and mapped TSX of Tunabreen (b) from May 5th 2013. The TSX image is very dark, and features like crevasses are hard to identify compared to the summer image in Figure 5.4a. This is caused by low backscatter, when microwaves are absorbed by a wet surface. The mapped terminal crevasse field is smaller in the summer image in Figure 5.3b compared to the mapped terminal crevasse field in the winter image in Figure 5.4b.

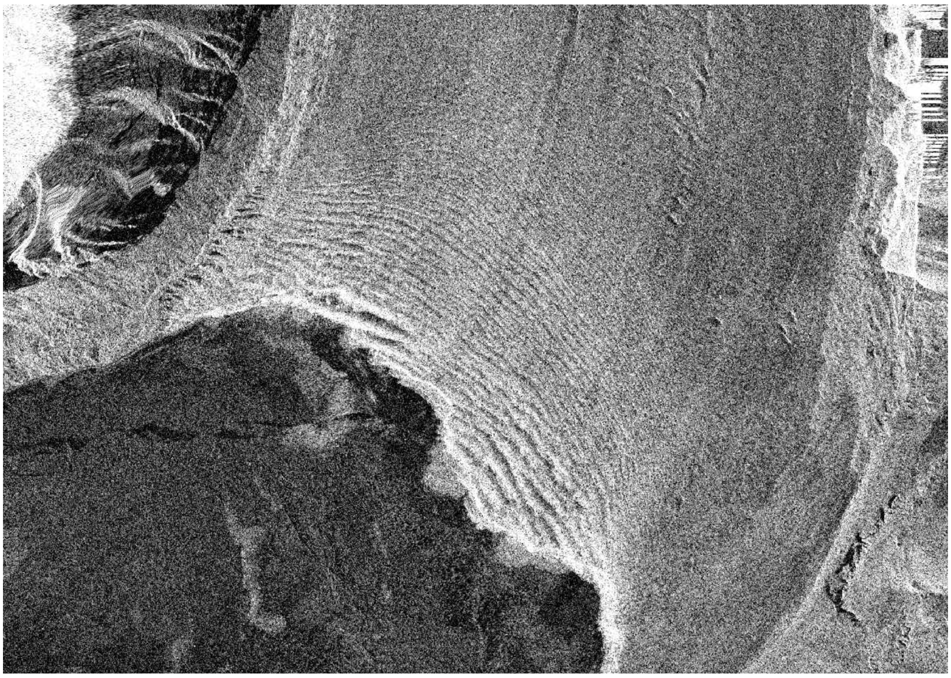

(a) Original TSX image.

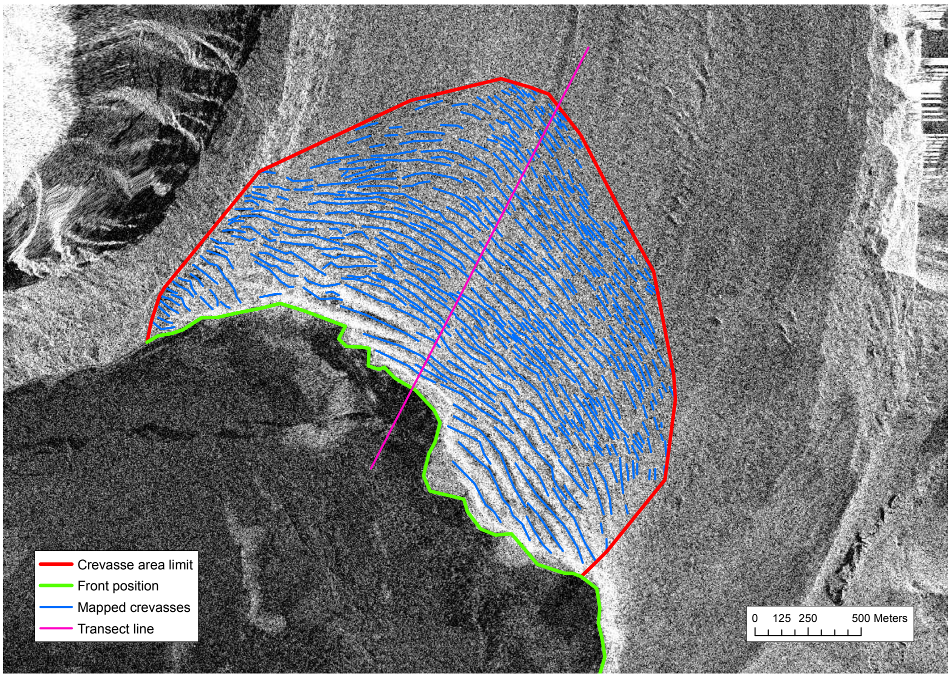

(b) TSX image including mapped crevasses, crevasse limit line, front position and transect line.

Figure 5.4: Raw TSX image (a) and mapped TSX of Tunabreen (b) from January 1^{st} 2014. The high backscatter gives a brighter image in Figure 5.4a, and features such as crevasses are easily identified in a greater extent compared to the summer image Figure 5.3a. The mapped terminal crevasse field in the winter image in Figure 5.4b is larger compared to the mapped terminal crevasse field in the summer image in Figure 5.3b.

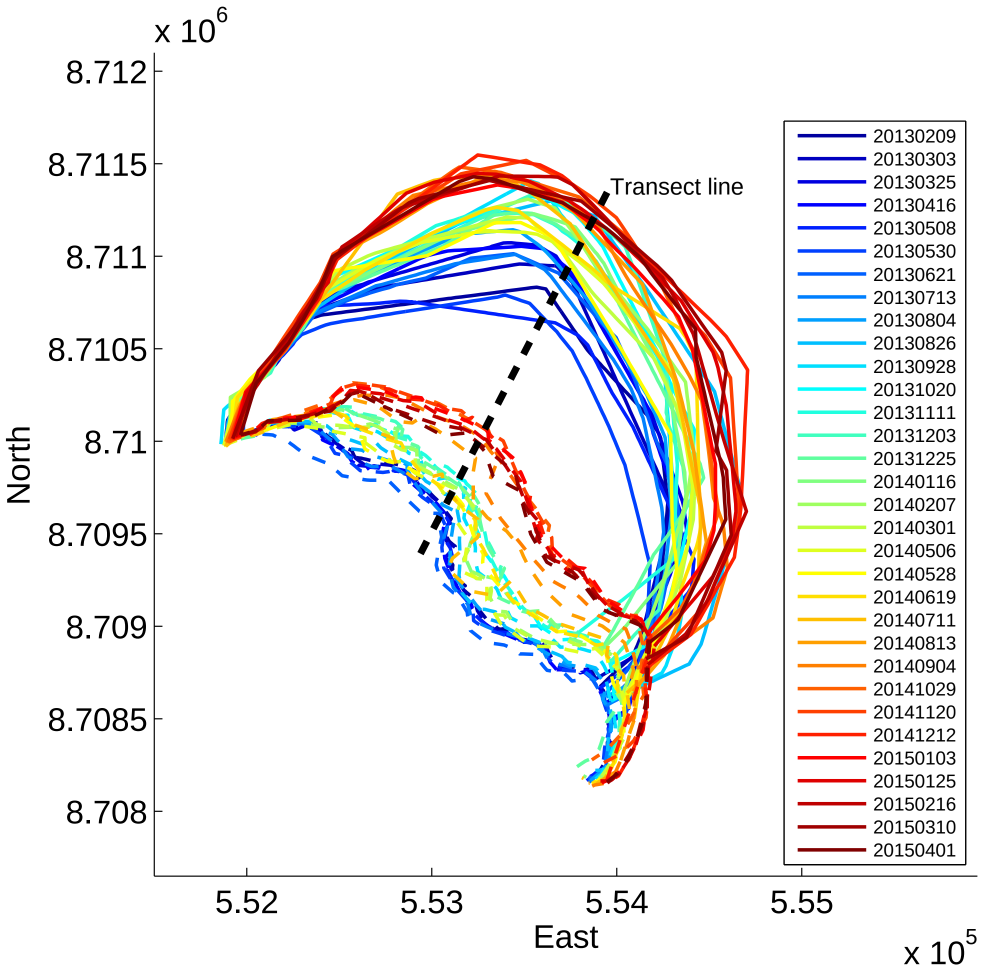

Figure 5.5: UTM plot including the crevasse limit lines and the front position lines of Tunabreen from February 9th 2013 to April 1st 2015. The dotted black line indicates the transect line used to visualize the position of front position and crevasse field limit line through time in Figure 5.8. The crevasse limit lines are coloured solid lines, and the front position is coloured dotted lines. The dates and associated colours are presented in the legend. The UTM coordinates (WGS84 zone 33 north) are given as Northing (y-axis) and Easting (x-axis).

line is more oscillating, but a clear up-glacier propagation can be seen from May to August 2013 and from May to November 2014. This is corresponding to the front position retreat, but the crevasse field is starting to propagate up-glacier before the front position starts retreating. In addition to the observed retreat periods, three periods of still-stand or minor advance of the front position can be seen on the plot in Figure 5.5. From February to May 2013, the front position is almost stationary and advances slightly towards the end of the period. In the two periods from October 2013 to May 2014 and from October 2014 to April 2015, the same trend can be seen. When looking at the crevasse area limit line, this is generally more oscillating and minor changes are hard to extract from the plot.

To investigate closer the relationship between the front line position and the crevasse area limit line, the UTM plot is divided into two separate periods; Winter 1 and Win-

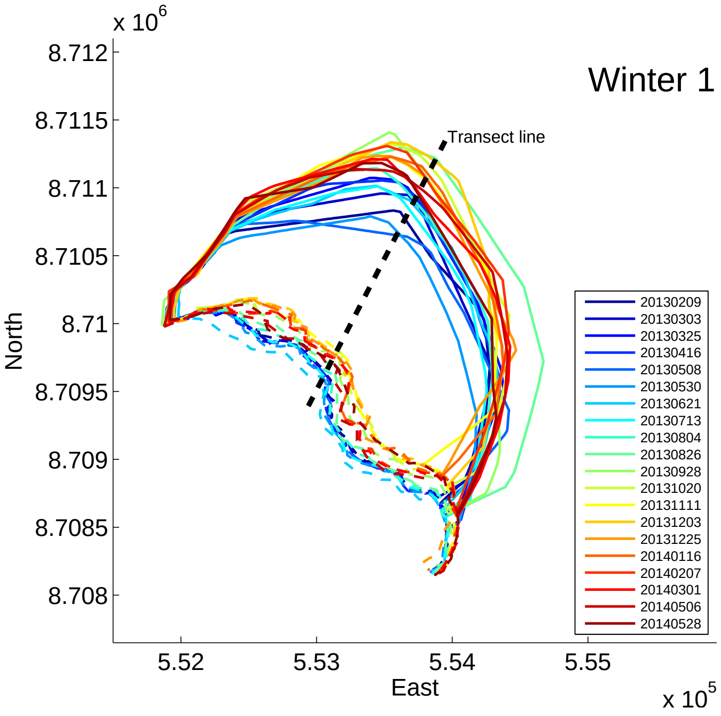

Figure 5.6: UTM plot including the crevasse area limit line and the front position of Tunabreen from February 9th 2013 to May 28th 2014. See Figure 5.5 for detailed caption.

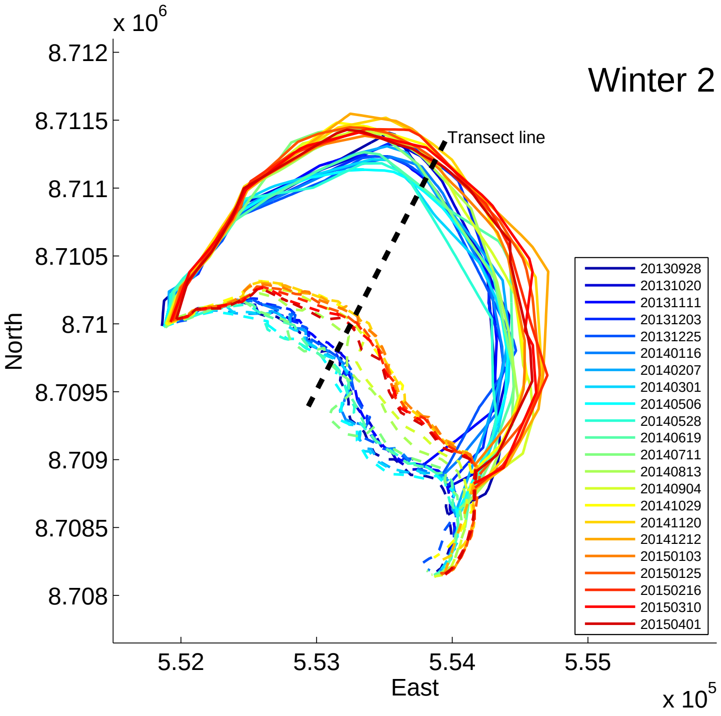

Figure 5.7: UTM plot including the crevasse area limit line and the front position of Tunabreen from September 28th 2013 to April 1st 2015. See Figure 5.5 for detailed caption.

ter 2. Winter 1 is presented in Figure 5.6, and comprises the period from February 9th 2013 to May 28th 2014. Winter 2 is presented in Figure 5.7, and comprises the period from September 28th 2013 to April 1st 2015. Winter 1 (Figure 5.6) confirms the trend of front line still-stand during winter and a minor advance during spring, in addition to a retreat during summer. When looking at the crevasse area limit line, this is propagating up-glacier during spring and summer, and stabilizes during the winter period. An important observation is that the crevasse area is larger in February 2014 compared to one year earlier, in February 2013. Winter 2 (Figure 5.7) shows clearly the distinct front line retreat during summer/fall 2014. In addition, the crevasse field propagates down-glacier during spring, and up-glacier continuously during summer and stabilizes during the winter period.

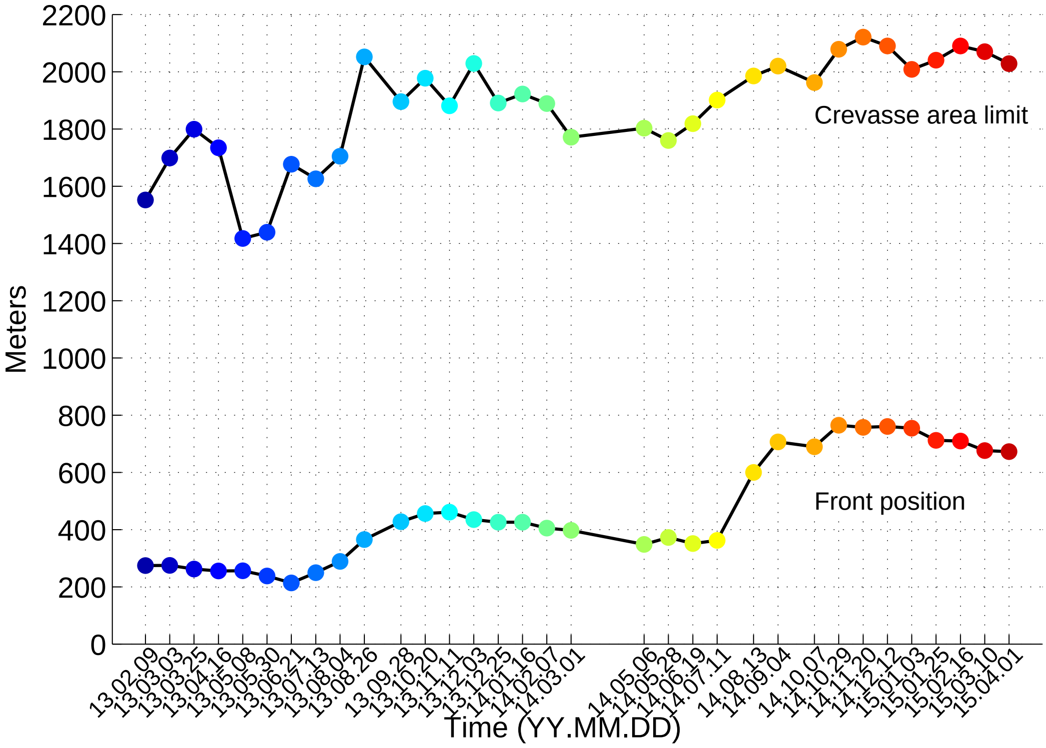

Figure 5.8: Time-distance diagram of the crevasse area limit line and glacier front position, made of a transect on the UTM plot in Figure 5.5. The colours of the points reflect the date of the image as described in the legend in Figure 5.5. The y-axis gives the distance in meter from a point in the fjord in front of the glacier, and the x-axis gives the dates of the mapped TSX images.

Figure 5.8 is a time/distance diagram based on the transect line in the UTM plot (Figure 5.5). The lower line represent the glacier front position line and the upper line represent the crevasse area limit line. The y-axis gives the distance in metres from a point in the fjord in front of the glacier, and the x-axis gives the dates of the mapped TSX images. The colours represent the corresponding front line/crevasse area limit line in Figure 5.5. The diagram shows the evolution of the front line and crevasse area limit line at one specific point through time, and support the observations in the UTM plots (Figure 5.5, 5.6 and 5.7). The step-by-step movement of the front line is clearly represented in this diagram. The up-glacier propagation of the crevasse area limit line during summer and the stabilization during the winter follow the front line trend. For the presented period from February 9th 2013 to April 1st 2015, the glacier front retreats 400 metres in total. The crevasse area limit line is propagating up-glacier by 450 metres. Dividing it into annual cycles, the retreat of the glacier front is 200 metres the first summer (June to October 2013), and 450 metres the second summer (July to October 2014). The crevasse area limit line does not follow the exactly same cycle as the front line regarding up-glacier propagation. The up-glacier propagation of the crevasse area limit in 2013 starts in May and ends in August, with an increase of 500 metres up-glacier during this period. In 2014, it starts in May and ends in November, with an increase of 300 metres.

5.3 Glacier velocities and strain rates

The selected velocity maps and 1st principal strain rate maps from Tunabreen used in this study are presented in Figure 5.9 and Figure 5.10. They are from three separate 11-day cycles; February 9th to 20th 2013, October 10th to 20th 2013 and December 3rd to 14th 2013. This is specified in the caption under each subfigure. The velocity maps display velocities between 0 and 1.0 m day^{-1}, concentrated to the glacier front area and the lower part of the crevasse area. Areas containing no calculated velocity are presented as gray areas. The white areas represent areas with a velocity of more than 1.0 m day^{-1}. All the three strain rate maps display strain rates between -0.1 and 1.0 day^{-1} × 10^{-3}. This is visualized by red to pink transverse lines of high strain rate, particularly seen in Figure 5.10a and Figure 5.10c. Grey to white areas are areas where no strain rate have been calculated.

Three velocity plots from the three selected time periods are presented in Figure 5.11. The values of calculated velocity vary from 0 to 1.0 m day^{-1}. Values of more than 1.0 m day^{-1} are displayed as white areas in the velocity maps. Maximum velocity values are given as 1.0 m day^{-1}. The trend in all the three plots is that the velocity is highest near the front and decreases up-glacier. All the extracted velocities are found in the lower part of the crevasse areas. There are no velocity measurements in the upper half of the terminal crevasse areas.

The velocity plot in Figure 5.11a from February 2013 contains 7 data points. The highest velocity is found 150 meter up-glacier from the front at 0.4 m day^{-1}, before it starts decreasing towards 0.1 m day^{-1} 500 m up-glacier from the front. The upper part of the crevasse area contains no values for glacier velocities. The velocity plot in Figure 5.11b from October 2013 contains 11 data points. The highest velocity is found closest to the front, with a sudden decrease in velocity up-glacier. From 500 to 800 meters from the front, the velocity remains stable on 0.1 m day^{-1}. The upper part of the crevasse area contains no values for glacier velocities. The velocity plot in Figure 5.11c from December 2013 shows the same trend as the two other velocity plots. It contains 16 data points, and the highest velocity is 0.7 m day^{-1} at the front line. The decreasing trend in velocity up-glacier is not as sudden as in Figure 5.11b, and the area of extracted velocity is larger compared to the two other plots. At 800 meters up-glacier from the front, the velocity is 0.1 m day^{-1}. As for the two other plots, the upper part of the crevasse area contains no values for glacier velocities.

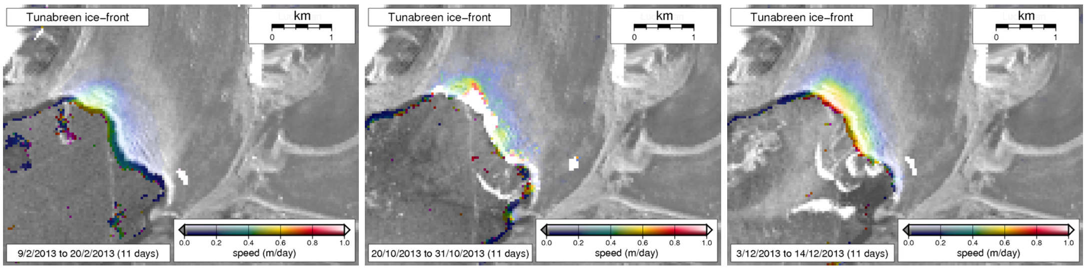

(a) February 9th to 20th 2013 **(b)** October 20th to 31st 2013 **(c)** December 3rd to 14th 2013

Figure 5.9: Velocity maps from Tunabreen based on TSX images provided by professor Adrian Luckman (Swansea University). The velocity is from a 11-day period, specific time intervals are given in the caption under each subfigure.

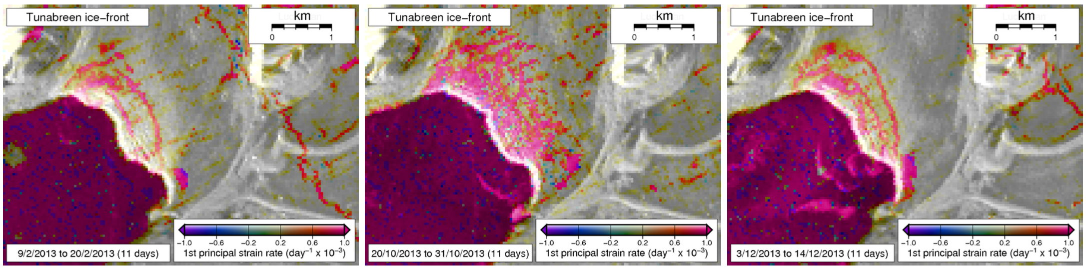

(a) February 9th to 20th 2013 **(b)** October 20th to 31st 2013 **(c)** December 3rd to 14th 2013

Figure 5.10: Strain rate maps from Tunabreen based on TSX images provided by professor Adrian Luckman (Swansea University). The 1st principal strain rate is from a 11-day period, specific time intervals are given in the caption under each subfigure.

Three strain rate plots from the three selected time periods are presented in Figure 5.12. Common for all the three strain rate plots are a varying strain rate, from 0.2 to 1.0 day^{-1} × 10^{-3}. In addition, the strain rate ends up at 0.2 day^{-1} × 10^{-3} close to or at the crevasse area limit line in two of the time periods. The strain rate plot from February 2013 (Fig. 5.12a) has less data points compared to the two other plots. This can also be seen from the strain rate map in Figure 5.10a, which contains larger areas of non-calculated strain rates compared to the two other strain rate maps.

The strain rate plot in Figure 5.12a from February 2013 contains 10 data points. All the points are within the values of 0.1 to 1.0 day^{-1} × 10^{-3}, and the highest strain rate values are found in the lower half of the crevasse area. The upper half of the crevasse area only contain values of strain rate from 0.1 to 0.4 day^{-1} × 10^{-3}. The strain rate closest to the crevasse area limit line is 0.4 day^{-1} × 10^{-3}. The strain rate plot in Figure 5.12b from October 2013 contains 20 data points, within the values of 0.2 to 1.0 day^{-1} × 10^{-3}. There is no clear trend in increase or decrease of strain rate from the front towards the crevasse area limit. The strain rate value at the crevasse area limit line is 0.2 day^{-1} × 10^{-3}. The strain rate plot from December in Figure 5.12c contains

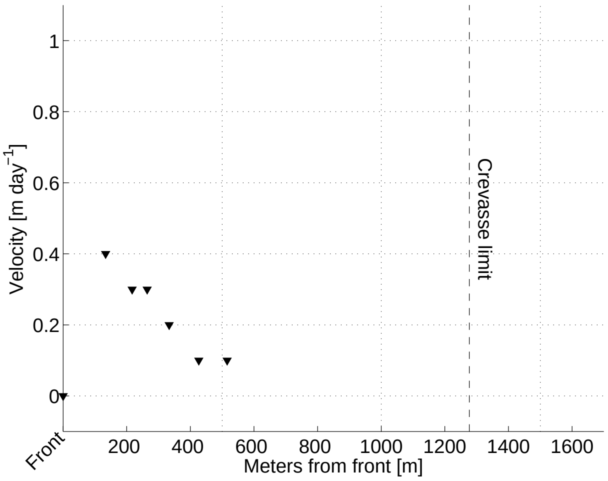

(**a**) February 9th to 20th 2013

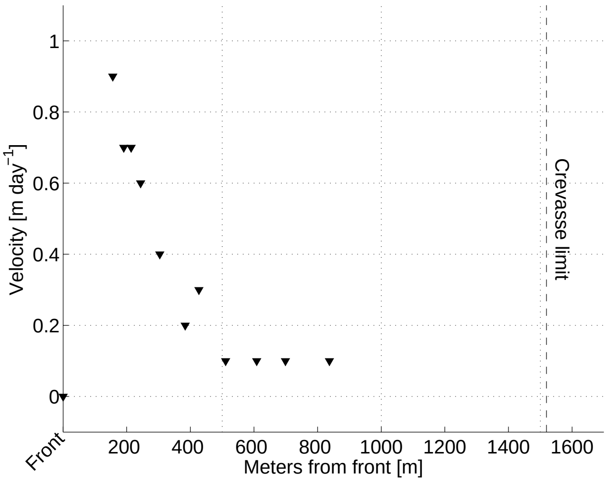

(**b**) October 10th to 20th 2013

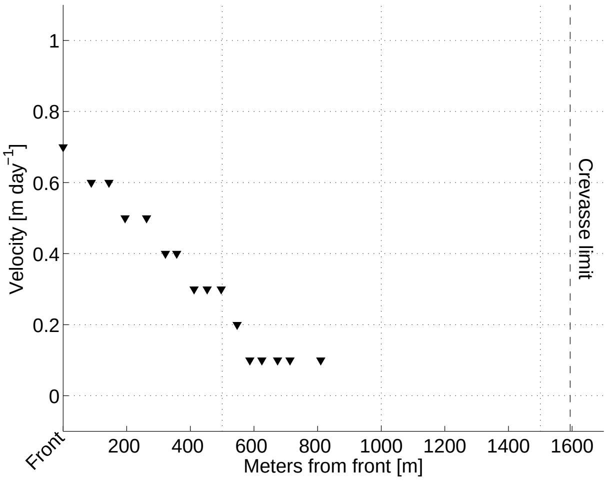

(**c**) December 3rd to 14th 2013

Figure 5.11: The glacier velocity plotted along a transect from the glacier front to the crevasse area limit. The strain rate is extracted from the velocity map in Figure 5.9. The front line and crevasse limit line positions used is from mapped TSX images from the same period as the velocity maps.

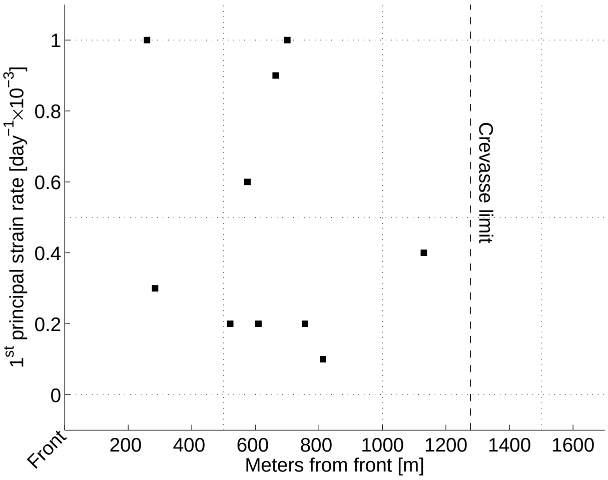

(**a**) February 9th to 20th 2013

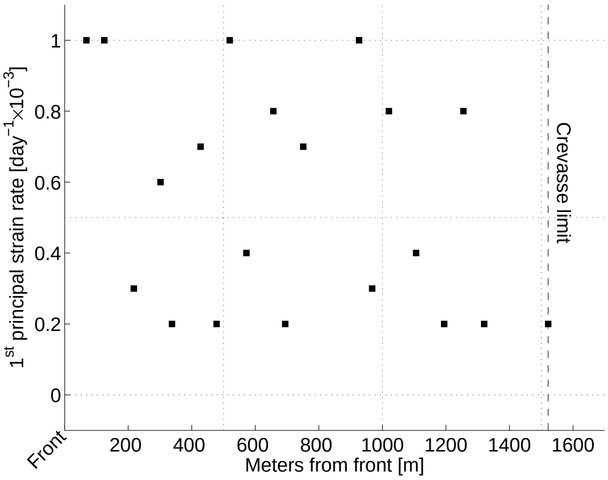

(**b**) October 10th to 20th 2013

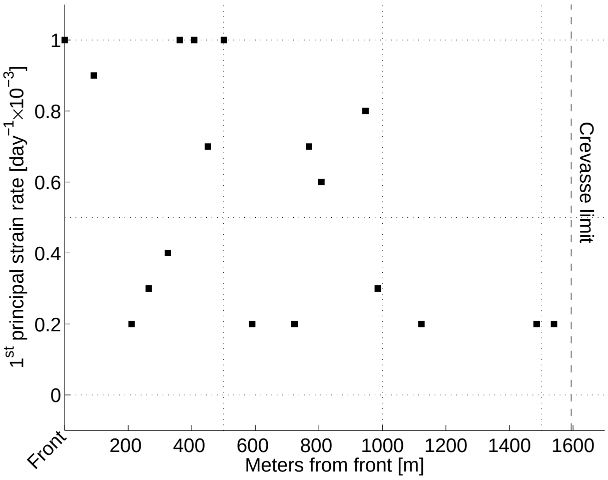

(**c**) December 3rd to 14th 2013

Figure 5.12: The 1st principal strain rate plotted along a transect from the glacier front to the crevasse area limit. The strain rate is extracted from the strain rate maps in Figure 5.10. The front line and crevasse limit line positions used is from mapped TSX images from the same period as the strain maps.

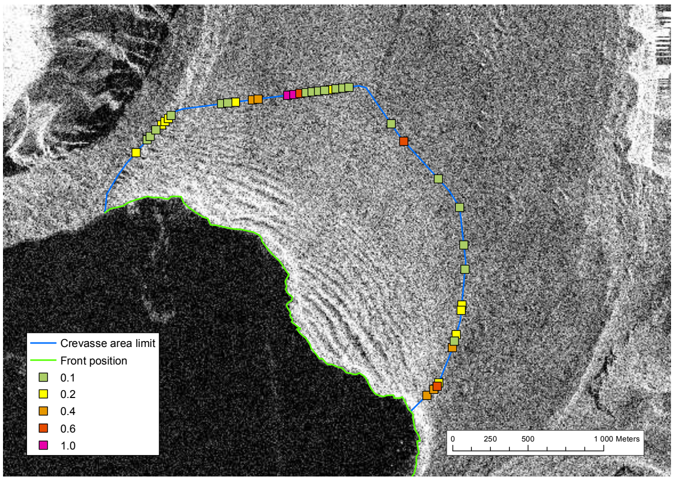

(a) February 9th 2013

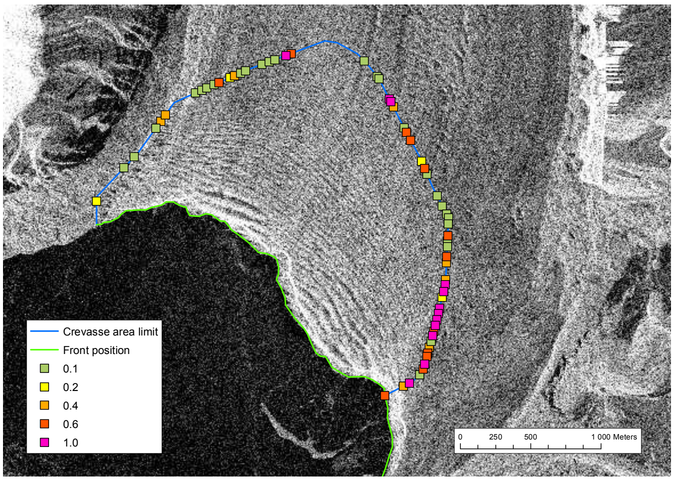

(b) October 10th 2013

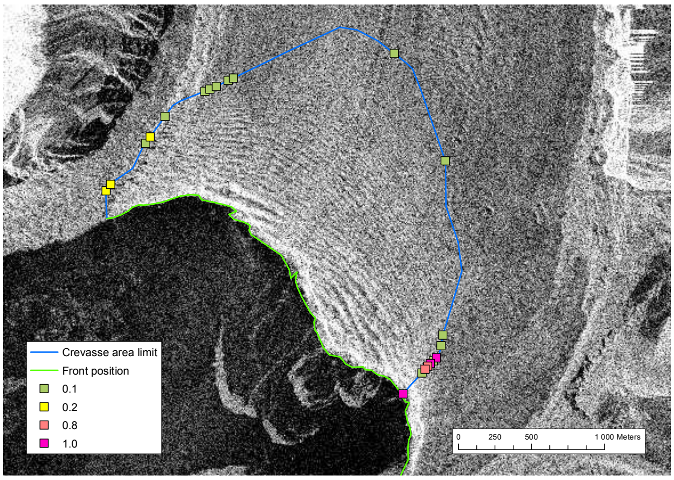

(c) December 3rd 2013

Figure 5.13: The 1st principle strain rate plotted along the crevasse area limit line as coloured squares. The strain rate is extracted from the corresponding strain rate map in Figure 5.10. The base layer image, front line position (green line) and crevasse limit line position (blue line) used are from a mapped TSX image from the date as listed in the subcaptions.

18 data points within the values of 0.2 to 1.0 $\text{day}^{-1} \times 10^{-3}$. The highest strain rate calculated is found in the lower part of the crevasse field. The strain rate increases up-glacier towards the crevasse area limit, and the strain rate closest to the crevasse area limit is 0.2 $\text{day}^{-1} \times 10^{-3}$.

In addition to the strain plots, strain rate maps containing strain rate extracted along the crevasse area limit line are presented in Figure 5.13. The crevasse area limit line is blue, the glacier front line is green, and the strain rate values and corresponding colors are defined in the legend. The highest strain rate found along the crevasse area limit line is 1.0 $\text{day}^{-1} \times 10^{-3}$ and higher (pink squares). Some parts along the line have no calculated strain rate. The strain rate map from October 10th to 20th 2013 in Figure 5.13b has the largest amount of strain rate measurements along the crevasse area limit line. The smallest amount of strain rate measurements is found in the strain rate map from December 3rd to 14th 2013 in Figure 5.13c. Common for all three maps is that the dominating strain rate along the part of the crevasse area limit line furthest away from the glacier front is 0.1 $\text{day}^{-1} \times 10^{-3}$ (green squares).

The crevasse area of Austre Torellbreen has been mapped, to compare with the crevasse extent and velocities of Tunabreen. The TSX image used for mapping of Austre Torellbreen is from February 13th 2013, and the crevasse map is presented in Figure 5.15. As seen on this figure, the mapped crevasses (blue lines) on Austre Torellbreen extends from the glacier front and about 6 kilometers up-glacier. The crevasse area limit line (red line) is drawn from the glacier front (green line) to the area where the glacier meets with the Vrangpeisbreen glacier in the southeast. To compare with the crevasse map, a velocity map of Austre Torellbreen is presented in Figure 5.15. The velocity map is from the period February 13th to 24th 2013, and is displaying velocities between 0 and 2.0 m day^{-1}. Areas containing no calculated velocity are presented as gray areas. The white areas represent areas with a velocity of more than 2.0 m day^{-1}. The highest velocity is detected closest to the front of the glacier, represented by colours of pink to yellow and green (~0.8 to ~2.0 m day^{-1}). Large parts of the area with detected velocity are blue to green, given the velocities from ~0.1 to ~0.9 m day^{-1}. The area of detected velocity extends from the glacier front to about 5 km up-glacier.

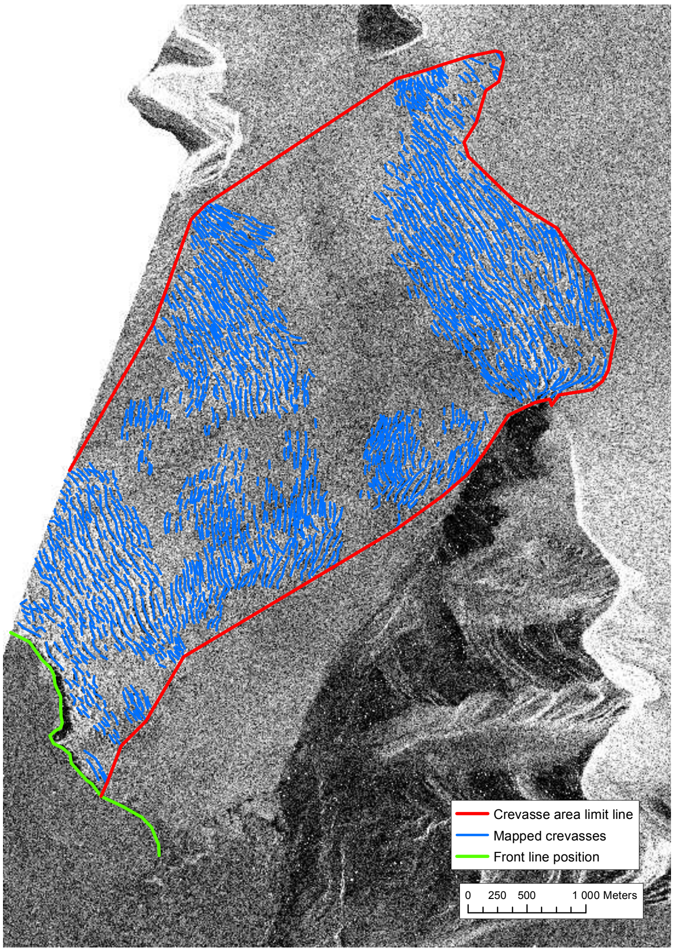

Figure 5.14: Crevasse map of Austre Torellbreen from February 13th 2013. The crevasse map only includes the area where velocity is detected, as seen in the lower left corner on the velocity map in Figure 5.15.

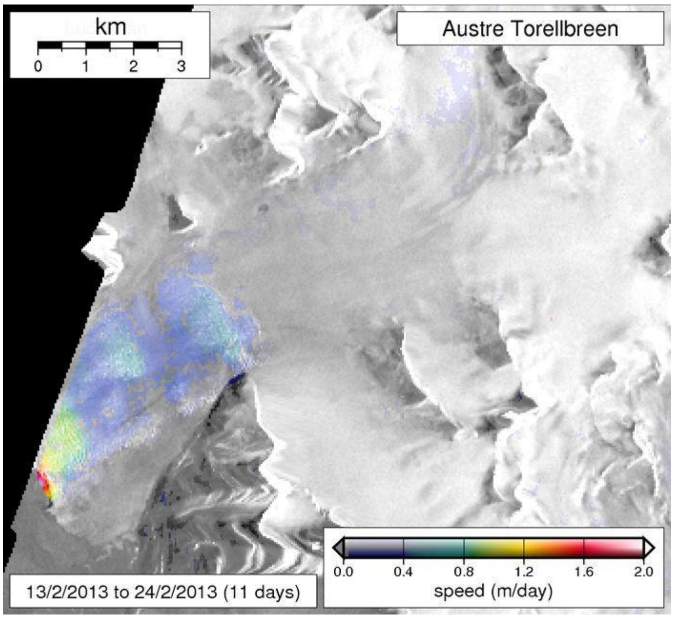

Figure 5.15: Velocity map of Austre Torellbreen from February 13th to 24th 2013. Austre Torellbreen is the glacier in the lower left area, where velocity is detected.

CHAPTER

6

DISCUSSION

In this, the results presented in Chapter 5 will be discussed. First, the results from the field measurements will be compared to the manual mapping of the TSX images in ArcMap. Secondly, the UTM plot and time/distance diagram and their relation will be discussed. Finally, the velocity and strain rate plots will be compared to the results from the terminal crevasse field mapping. In addition, the safety aspect of using TSX images to map crevasse areas is included.

6.1 Field measurements and crevasse mapping in ArcMap

The two glaciers used for ground measurements in this study, Borebreen and Tunabreen, are both tidewater glaciers and defined as surge-type glaciers currently in their quiescent phase. Their terminal crevasse fields have different characteristics in terms of size, shape, crevasse width and crevasse density. The crevasses measured on Borebreen are generally narrower compared to the crevasses measured on Tunabreen. In addition, the density of crevasses is higher in the upper, outer part of the crevasse field on Tunabreen compared to Borebreen. On Tunabreen, the widest crevasses (class 3 and 4) are mainly found along the limit line of the crevasse field. On Borebreen, the widest crevasses are mostly situated well inside the mapped crevasse area.

As seen on the crevasse map of Borebreen in Figure 5.2, some areas within the mapped crevasse field does not contain any crevasses. This is confirmed by the field observations , and no crevasses are observed and measured in these areas. On Tunabreen, there are also some areas within the mapped crevasse field that does not contain any mapped crevasses. The field measurements show that there are crevasses of class 2 and 3 in this area that does not appear on the TSX image. One reason for this can be because of the deviation between the measured coordinates in the field and the coordinates of the mapped crevasses on the TSX image explained in

Section 4.3. Another reason could be that the resolution of the TSX stripmap image is not sufficient to identify all possible crevasses. All the measured crevasses on both glaciers are situated within the mapped terminal crevasse area.

The limitation of mapping crevasses on TSX images in ArcMap is mainly restricted to two important factors; high and low backscatter caused by different temperature and surface conditions. Low backscatter images are a result of wet snow or water on the glacier surface during melt periods. These occur on the images from spring and summer, and gives dark images. The low backscatter may prevent the identification of the small and narrow crevasses in the upper and outer part of the terminal crevasse field. This is exemplified in Figure 5.3. In addition, the time/distance diagram in Figure 5.8 shows a drastic down-glacier shift of the limit of the crevasse area during May 2013. This may be caused by low backscatter images reducing the ability to identify smaller crevasses in the upper and outer part of the terminal crevasse area. It is reasonable to believe that the crevasse area is slightly larger than showed in Figure 5.8 at this time. High backscatter images are a result of dry surface conditions and snow accumulation. When snow accumulates on the glacier during the winter, this can lead to high backscatter and transparent images. Transparent images can smooth out the crevasses, and lead to an interpreted crevasse field which is less extensive than it actually is. The variable position of the crevasse area limit line during winter in Figure 5.8 may reflect this effect. The crevasse area limit line is oscillating in a 100 meter interval during winter 2013/2014, and this trend can be seen during winter 2014/2015 as well. This can indicate periods of heavy snowfall or periods of low surface temperatures causing variable surface transparency and an interpreted crevasse field of reduced size.

Based on the field measurements and the manual crevasse mapping in this study, it can be concluded that the TSX images are a suitable tool for defining crevasse areas on glaciers. The resolution of the used stripmap mode images and the less accurate correspondence to ground coordinates gives the method a weakness in terms of identifying all the small and narrow crevasses in the outer parts of a crevasse field. The method is not confirmed to be accurate enough for individual crevasse mapping, but is indeed suitable for defining terminal crevasse fields and other larger crevasse areas. The area of measured crevasses on both glaciers only covers a part of the large terminal crevasse area. The ground measurements are focused on the outer part of the mapped crevasses and along the limit of the terminal crevasse area. This is where the crevasses are narrower and this gives a good test of the accuracy of crevasse field mapping using TSX images.

6.2 Fluctuations of front position and crevasse area limit

The UTM plot of the crevasse area limit line and the front position line in Figure 5.5 gives a good visualization of the fluctuations during almost two winter-to-winter cycles. The data shows that the retreat of the front line corresponds with an up-glacier propagation of the crevasse field. This up-glacier propagation of the terminal crevasse field can be more easily detected in the two separate periods from Winter 1 in Figure 5.6 and Winter 2 in Figure 5.7. As seen in the Winter 1 period in Figure 5.6, the crevasse area limit line is migrating up-glacier during spring, and its maximum extent is found in late August. The crevasse area limit is stabilizing during fall and winter, and minimize its extent compared to the late-summer extent. The position of the crevasse area limit line is further up-glacier in February 2014 compared to its position in February 2013. This can probably be related to a retreat of the glacier during the summer season. The ice velocities typically increase towards the terminus of a calving glacier, and this downstream increase in the velocity stretches the ice (Benn et al., 2007a). This stretching can potentially open surface crevasses transverse to flow, and in this way the crevasse area will propagate up-glacier in response to a retreat of the glacier front. The terminal crevasse field will propagate up-glacier as the front is calving back. This trend is also seen in the Winter 2 period in Figure 5.7. In Winter 2 a rapid retreat of the glacier front can be seen during summer 2014. A trend of up-glacier migration of the crevasse area during the same time period can be observed as well. The maximum extent of the terminal crevasse field during Winter 2 is hard to extract from Figure 5.7, as the crevasse area seems to keep its large extent during the following winter. It does not decrease in extent as it did during fall and winter in Winter 1.

The time/distance diagram in Figure 5.8 shows the trend of a crevasse field propagating up-glacier during spring and summer, and stabilizes during fall and winter. This is followed by the glacier front, which tends to stand still or slightly advance during winter and retreat distinctly during summer. As seen in the diagram, the crevasse field starts to propagate before the front starts retreating. This can be interpreted as a melt water signal when water pours into crevasses when melting starts in the spring. As explained in Section 2.1.2 by Equation 2.5 from Benn et al. (2007a), a crevasse will penetrate deeper and grow wider when adding water, due to the water pressure acting in the same direction as the longitudinal tensile stress tending to pull the crevasse apart. Narrow crevasses growing wider and larger along or outside the mapped crevasse area are more likely to appear on the TSX images during this period. Hence, the crevasse area grows larger.

The retreat of the front line during the period of investigation can be divided into two sub-periods. From June to October 2013, the front retreats about 250 meters, before it stabilizes and slightly advances throughout the fall and winter. A new retreat takes place from July to October 2014, and the glacier calves back about 400 meters during this period. This is twice as much as the retreat the previous year. This seasonal pattern of a modestly advance during winter and strong retreat during summer corresponds with the observations in the study of Tunabreen by Luckman et al. (in review). Figure 6.1 illustrate the frontal ablation rate and its two key components: the rate of change of ice front position and the terminus speed. This data is derived from the similar TerraSAR-X images as used in this study, but in a 11-day cycle giving a higher temporal resolution. The blue line indicating the mean ice front position and the orange line indicating the mean retreat line, show a front retreat during summer and a modestly advance during winter. This trend is corresponding with the trend observed in Figure 5.8. In a study from 2012, Mansell et al. investigates the changes in the surge faces of four tidewater-terminating glaciers in northwest Svalbard in a 20 year time series. An observed trend during the quiescence phase was a seasonal oscillation in the calving front. During summer the terminus retreat rates increased, and during winter the retreat rates were restricted or terminus advance took place. The observations by Mansell et al. (2012) and Luckman et al. (in review) are similar to the observations done in this study, and the three studies combined can possibly confirm this trend as general for surge-type tidewater glaciers in their quiescent phase.

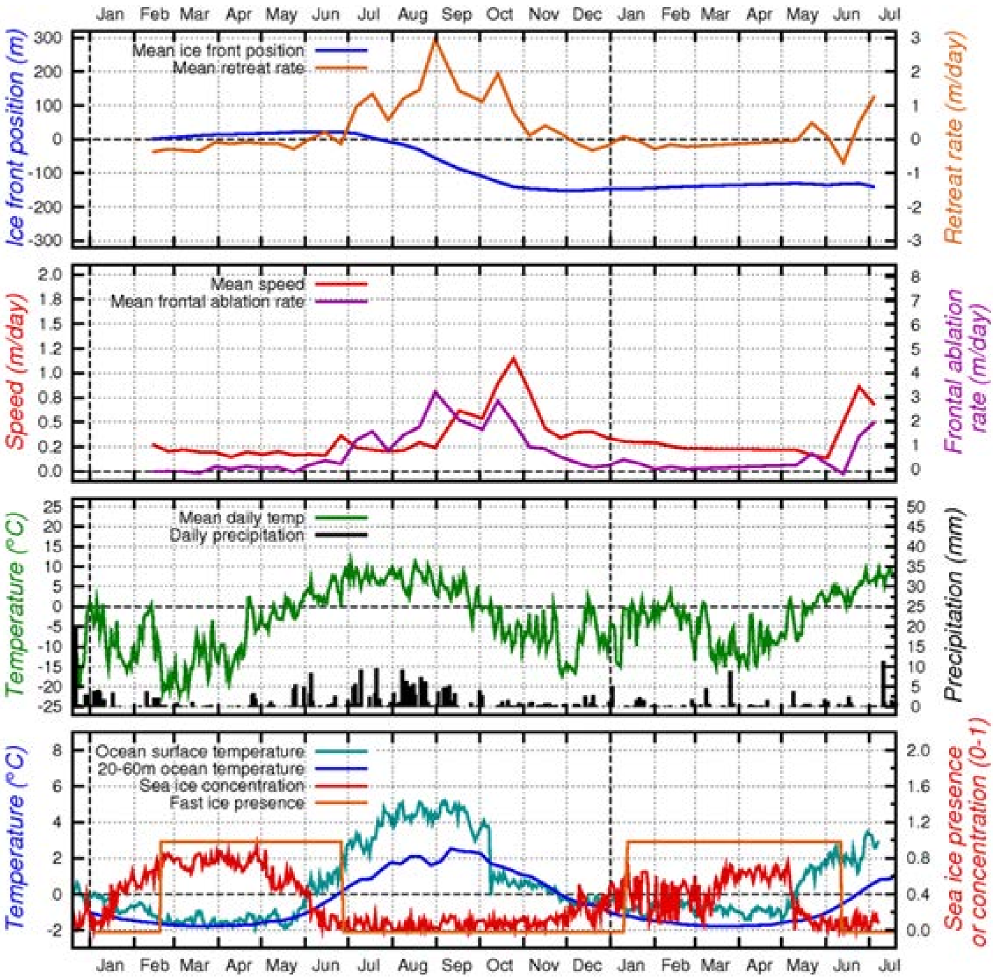

Figure 6.1: Data derived from a series of 11-day repeat TerraSAR-X images from 2013 and 2014 for Tunabreen to illustrate the frontal ablation rate and its two key components: the rate of change of ice front position and the terminus speed. Temperature and precipitation from the weather station in Longyearbyen is shown, as well as ocean temperatures and sea ice concentrations. From Luckman et al. (in review).

The crevasse area limit line is not following the exact trend as the front position line. It is reasonable to believe that the extent of the crevasse area in May 2013 is slightly larger than the illustrated position in Figure 5.8 at this time. As previously discussed, the low backscatter images from this period may prevent the identification of the narrowest crevasses in the upper part of the terminal crevasse field because of high temperatures and high melt. The correct position of the crevasse area limit line will probably be at around 1600 meters. This will give a up-glacier propagation from May to August 2013 of 450 meters. During the following year, the crevasse area propagates up-glacier with 300 meters from May to November 2014. It is important to note that the time/distance diagram is only based on one transect line, and that the variations probably will be different if measurements were done at other transects on the glacier. The numbers extracted from the diagram will only indicate a trend for the general glacier behaviour, and cannot be used as exact numbers to calculate i.e. glacier velocity.

6.3 Velocity and strain rate thresholds related to crevasse formation

The velocity maps in Figure 5.9 were used to extract the values of velocity in a transect from the glacier front to the crevasse area limit as displayed in the velocity plots in Figure 5.11. The velocity maps and the velocity plots only contain velocity information from the lower part of the terminal crevasse field. Luckman et al. (in review) also confined the detectable motion to the frontal zone on Tunabreen, where high longitudinal stress gradients induce outward stretching of the ice. By comparing the three velocity plots, it can be observed that the area containing velocity information is smallest in January 2013, and at this time the crevasse area limit line is closest to the front as well (Figure 5.11a). The area containing velocity information is largest in December 2013 when the crevasse area is the largest (Figure 5.11c). In addition, it can be observed that the area of velocity information only covers the lower half of the crevasse area in all three plots. This can also be seen in the velocity maps in Figure 5.9, where the coloured areas of measured velocity are confined to the areas close to the glacier front. It is reasonable to believe that there are movement in areas further up-glacier, based on the information from the crevasse maps and the field measurements. Field measurements and crevasse mapping show that the extent of the crevasse field is larger than the area of measured velocity in the calculated velocity maps in Figure 5.9. This means that movement in the upper part of the crevasse field is not detectable by using TSX images for feature tracking.

By using velocity maps of poor quality, it is hard to extract strain rate correctly. In Figure 5.10, the strain rate maps indicates lines of high strain rate. As discussed in Section 4.3, the lines of high strain in the winter strain maps are associated with the discontinuity problem in the feature tracking algorithm. This can be seen in Figure 5.12, where strain rate values are scattered all along the transect line from the front to the crevasse area limit in all the three plots. This means that the reliability of the strain rate values used in the strain rate plots are considered to be low. In two of three strain rate plots the strain rate along or close to the crevasse area limit line is found to be 0.2 $\text{day}^{-1} \times 10^{-3}$. The values of 0.1 $\text{day}^{-1} \times 10^{-3}$ and 0.2 $\text{day}^{-1} \times 10^{-3}$ are also common to find along the crevasse area limit line in Figure 5.13. This can indicate

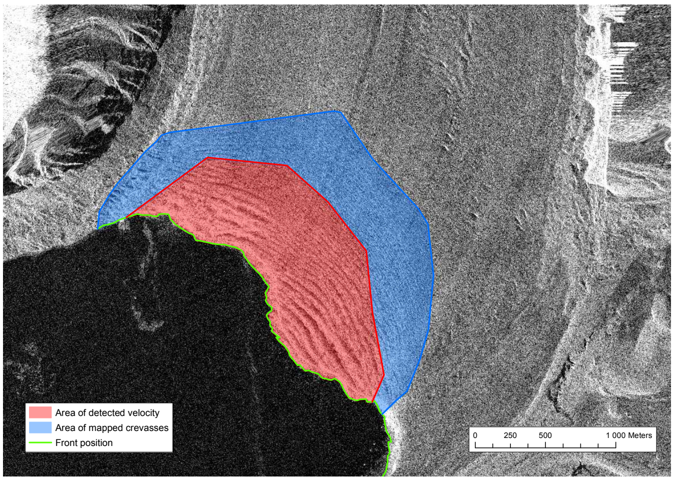

(a) February 9th 2013

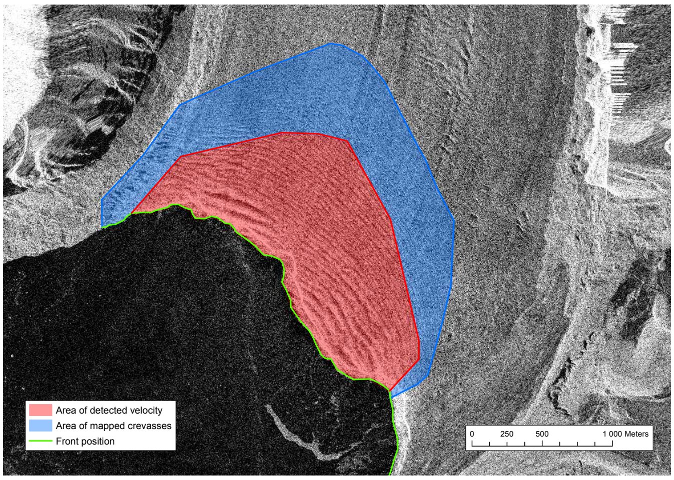

(b) October 10th 2013

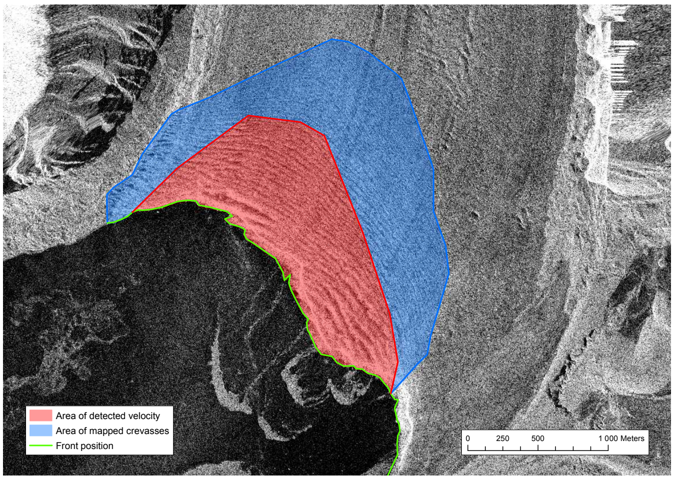

(c) December 3rd 2013

Figure 6.2: Illustrative figures of the difference in extent between the area of detected velocity (red) and the area of mapped crevasses (blue) in three selected time periods. The figures are based on crevasse maps from the listed dates and the velocity maps presented in Figure 5.9.

that the threshold strain rate for crevasse opening may be of 0.1 $\text{day}^{-1} \times 10^{-3}$ and 0.2 $\text{day}^{-1} \times 10^{-3}$ in this area of the glacier, but this is rather uncertain. The resolution of the data used in this study is not high enough to confirm this value. The measured strain rate can probably be a result of the opening of the crevasse, rather than a cause for it to open.

6.4 Crevasse mapping in a safety perspective

Crevasses are major hazards for travelers on Svalbard glaciers, and as previously mentioned, there is no systematic mapping of crevasse fields. This study has been aiming to determine if crevasse maps or velocity maps based on TerraSAR-X images can be used to indicate areas of high risk that should be avoided by glacier travelers. After an incident involving a tractor falling into a crevasse on the western side of the Ross Ice Shelf in Antarctica, the site was investigated by Whillans and Merry (2001). They used near infrared band Landsat and SPOT images, and did not identify any crevasses in the region where the tractor fell into a crevasse. The study concluded that crevasses exist in zones with small deformation rates, and that they were not detectable on the satellite images due to snow bridges. The TerraSAR-X microwave images used in this study allow identification of crevasses almost independent on physical conditions such as snow cover. It is shown that the TerraSAR-X images can be very useful to detect crevasses in areas with snow cover and small deformation rates, that is expected to be safe travel routes.

By mapping the terminal crevasse field of Tunabreen in two winter-to-winter cycles, and comparing its extent to the velocity maps provided by Adrian Luckman (Swansea University/UNIS) it is possible to tell if one or both of the methods will be good indicators of high risk areas to avoid. The velocity maps in Figure 5.9 and the velocity plots in Figure 5.11 shows that in some parts of the terminal crevasse area, no velocity is detected. To illustrate this better, the area of detected velocity is compared to the mapped crevasse area. In Figure 6.2, the area of detected velocity is added to crevasse maps from the same time period. All the three subfigures clearly indicate that the area of detected velocity does not have the similar extent as the mapped crevasse area. The area of detected velocity only covers about half of the area of mapped crevasses on Tunabreen.

By mapping the crevasse area of the fast-flowing Austre Torellbreen and compare the crevasse area extent to the extent of the area of detected velocity, the result is different. As seen on Figure 5.14, the area of mapped crevasses are extending far up-glacier, compared to the terminal crevasse field of Tunabreen and Borebreen. In the velocity map in Figure 5.15, the area of detected velocity is quite large and covers the lower half of the total glacier area. In Figure 6.3, the area of detected velocity on Austre Torellbreen is added to the crevasse map, and the crevasse area and velocity area nearly have extent. The crevasse area is slightly larger compared to the area of detected velocity.

The two different glaciers give various results when comparing velocity maps to crevasse area maps. The reason why the area of detected velocity is larger and more accurate in Austre Torellbreen, could be because this glacier is a well defined region of faster flowing ice, and will be more within the detection threshold. Usually on calving glaciers, the strain rates and glacier speeds starts very low up-glacier, and increases towards the front. This is seen on the velocity maps of Tunabreen in Figure 5.9. Austre Torellbreen is also a calving glacier, but if the ice here is moving faster in a larger region, the velocity will probably be more easily detected in the TSX images. From this, it is reasonable to exercise extreme caution when using velocity maps as an indicator for crevassed areas. The method is found to only work in some areas. If used, it should be taken into account that the crevassed area may be double the size of the area of detected velocity.

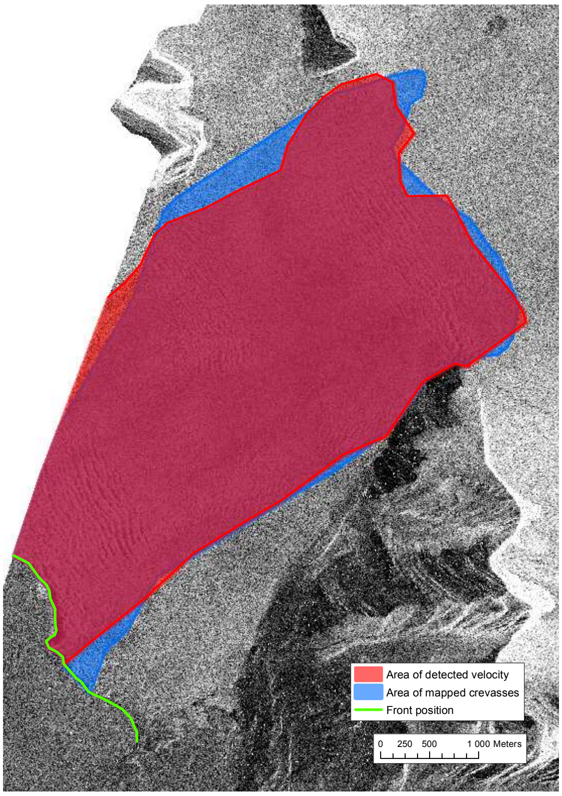

Figure 6.3: The difference in extent between the area of detected velocity (red) and the area of mapped crevasses (blue) on Austre Torellbreen in the period from February 13th to 24th 2013. The figure is based on the crevasse map from February 13th 2013 in Figure 5.14 and the corresponding velocity map in Figure 5.15.

CHAPTER 7

CONCLUSION

This work has tested the use of TerraSAR-X images as a reliable source for mapping glacier surface crevasses and defining crevasse areas. The data used for this was ground truth measurements from Tunabreen July 18th and Borebreen August 1st 2014, compared to manual mapped TSX images from the same time period. The development of the terminal crevasse field on Tunabreen has also been investigated during almost two winter-to-winter cycles, using a series of images in a 22-day cycle from February 9th 2013 to April 1st 2015. Furthermore, strain rate maps from three winter periods have been compared to the mapped crevasse images, to try extracting the threshold strain rate for crevasse opening. In addition, velocity maps have been compared to crevasse maps on both Tunabreen and Austre Torellbreen to see if velocity maps can be used as an indication of possible crevasse areas and their extent.

7.1 Concluding statements

The following concluding statements from this study can be made, based on the aims and objectives introduced in Chapter 1:

- The mapping of TSX images performs well compared with the ground observations made in the field. There are some restrictions, based on the fact that the TSX images lack quality when the backscatter is too high or too low. This happens most likely during periods of high melt in the spring/summer and during periods of snowfall and low temperatures in the fall/winter. These conditions can lead to an underestimation of the crevasse area extent.

- The terminal crevasse field migrates up-glacier during spring and summer, and stabilizes during the winter. This pattern coincides with the pattern of retreat and still stand or advance of the glacier front. The propagation of the crevasse field seems to start before the retreat of the glacier front.

- The strain rates extracted from strain rate maps produced by feature tracking of TSX images are not accurate enough to identify threshold strain rate for crevasse opening. It is not possible to define a threshold strain rate for crevasse opening from the used data in this study.

- The velocity mapping produced by feature tracking of TSX images only detects about half the size of the mapped terminal crevasse field on a surging glacier in its quiescent phase. It corresponds better with the mapped crevasse field on a fast-flowing glacier. The crevasses in the terminal crevasse field form way below the detected velocity threshold. The use of velocity maps as an indicator for crevassed areas work on some glaciers but not so well on others, and extreme caution is needed. If used, it should be taken into consideration that the crevassed area may be double the size of the area of detected velocity.

7.2 Improvements and future work

To further develop the method of mapping crevasses presented in this study, several improvements could be done. By using TerraSAR-X images of higher resolution, like the spotlight mode images giving a resolution up to 1 meter, smaller and narrower crevasses can be identified. The scene size of the spotlight mode images are smaller, but for limited areas like valley glaciers and glacier fronts this will give a more accurate and precise result. In addition, by testing the method on several glaciers it can be confirmed or not if the method is usable for various settings and conditions.

By developing an automatic classification method of crevasses in TerraSAR-X images, large areas can be mapped in a short time. The manual mapping of crevasse areas are time consuming, and an automatic method would be extremely useful for further investigations of crevasse areas and their distribution and development .

This study has proven that the data from velocity maps and strain rate maps based on feature tracking of TerraSAR-X images is not precise enough for detecting velocity in the entire crevasse area and extracting threshold strain rates for crevasse opening. By using strain meters, the opening of a crevasse can be measured over time. Field measurements of strain rates across the terminal crevasse field on Tunabreen can give a better insight into the crevasse formation and can be applied to the distribution pattern found for the terminal crevasse field through the two winter-to-winter cycles.

LIST OF FIGURES

LIST OF TABLES

BIBLIOGRAPHY

Bamber, J. L. (1987). Internal reflecting horizons in Spitsbergen glaciers. *Annals of Glaciology* 9, 5–10.

Benn, D. I. and Evans, D. J. A. (2010). Glaciers and Glaciation. *Hodder Arnold Publication,* 816 pp.

Benn, D. I., Hulton, N. R. J., and Mottram, R. H. (2007b). 'Calving laws', 'sliding laws' and the stability of tidewater glaciers. *Annals of Glaciology* 46, 123–130. DOI: `10.3189/172756407782871161`.

Benn, D. I., Warren, C. R., and Mottram, R. H. (2007a). Calving processes and the dynamics of calving glaciers. *Earth-Science Reviews* 82 (3), 143–179. DOI: `10.1016/j.earscirev.2007.02.002`.

Beszczynska-Möller, A., Fahrbach, E., Schauer, U., and Hansen, E. (2012). Variability in Atlantic water temperature and transport at the entrance to the Arctic Ocean, 1997–2010. *ICES Journal of Marine Science: Journal du Conseil.* DOI: `10.1093/icesjms/fss056`.

Blaszczyk, M., Jania, J. A., and Hagen, J. O. (2009). Tidewater glaciers of Svalbard: Recent changes and estimates of calving fluxes. *Polish Polar Research* 30 (2), 85–142. URL: `http://www.polar.pan.pl/ppr30/PPR30-085.pdf`.

Breit, H., Fritz, T., Balss, U., Lachaise, M., Niedermeier, A., and Vonavka, M. (2010). TerraSAR-X SAR Processing and Products. *Geoscience and Remote Sensing, IEEE Transactions on Geoscience and Remote Sensing* 48 (2), 727–740. ISSN: 0196-2892. DOI: `10.1109/TGRS.2009.2035497`.

De Geer, G. (1910). Guide de l'excursion au Spitsberg: Excursion A1 (Guide to excursions on Spitsbergen: Excursion A1). *Paper presented at XI International Geological Congress, Exec. Comm., Stockholm.*

Dowdeswell, J. A. (1989). On the nature of Svalbard icebergs. *Journal of Glaciology* 35, 224–234. URL: `http://www.igsoc.org/journal.old/35/120/igs_journal_vol35_issue120_pg224-234.pdf`.

Dowdeswell, J. A., Hamilton, G. S., and Hagen, J. O. (1991). The duration of the active phase on surge-type glaciers: contrasts between Svalbard and other regions. *Journal of Glaciology* 37 (127), 388–400. URL: `http://www.igsoc.org:8080/journal/37/127/igs_journal_vol37_issue127_pg388-400.pdf`.

Fleming, E. J., Lovell, H., Stevenson, C. T. E., Petronis, M. S., Benn, D. I., Hambrey, M. J., and Fairchild, I. J. (2013). Magnetic fabrics in the basal ice of a surge-type glacier. *Journal of Geophysical Research: Earth Surface* 118 (4), 2263–2278. DOI: `10.1002/jgrf.20144`.

Flink, A. E., Noormets, R., Kirchner, N., Benn, D. I., Luckman, A., and Lovell, A. (2015). The evolution of a submarine landform record following recent and multiple surges of Tunabreen glacier, Svalbard. *Quaternary Science Reviews* 108, 37–50. DOI: `doi:10.1016/j.quascirev.2014.11.006`.

Førland, E. J., R., B., Hanssen-Bauer, I., Haugen, J. E., and Skaugen, T. E. (2011). Temperature and Precipitation Development at Svalbard 1900–2100. *Advances in Meteorology* 2011, 14. DOI: `doi:10.1155/2011/893790`.

Forwick, M., Vorren, T. O., Hald, M., Korsun, S., Roh, Y., Vogt, C., and Yoo, K.-C. (2010). Spatial and temporal influence of glaciers and rivers on the sedimentary environment in Sassenfjorden and Tempelfjorden, Spitsbergen. *Geological Society of London Special Publications* 01/2010 (344(1)), 163–193. DOI: `10.1144/SP344.13`.

Hagen, J. O., Kohler, J., Melvold, K., and Winther, J.-G. (2003a). Glaciers in Svalbard: mass balance, runoff and freshwater flux. *Polar Research* 22 (2), 145–159. DOI: `10.1111/j.1751-8369.2003.tb00104.x`.

Hagen, J. O., Liestøl, O., Roland, E., and Jørgensen, T. (1993). Glacier atlas of Svalbard and Jan Mayen. *Meddelelser Nr. 129, Norsk Polar Institutt, Oslo,* 160 pp.

Hagen, J. O., Melvold, K., Pinglot, F., and Dowdeswell, J. A. (2003b). On the net balance of the Glaciers and Ice Caps in Svalbard, Norwegian Arctic. *Arctic, Antarctic and Alpine Research* 35 (2), 264–270. DOI: `10.1657/1523-0430(2003)035[0264:OTNMBO]2.0.CO;2`.

Hagen, J. O. and Sætrang, A. (1991). Radio-echo soundings of sub-polar glaciers with low-frequency radar. *Polar Research* 9 (1), 99–107. DOI: `10.1111/j.1751-8369.1991.tb00405.x`. URL: `http://dx.doi.org/10.1111/j.1751-8369.1991.tb00405.x`.

Hagen, J. O., Eiken, T., Kohler, J., and Melvold, K. (2005). Geometry changes on Svalbard glaciers: mass-balance or dynamic response? *Annals of Glaciology* 42 (1), 255–261. DOI: `doi:10.3189/172756405781812763`. URL: `http://www.ingentaconnect.com/content/igsoc/agl/2005/00000042/00000001/art00038`.

Hambrey, M. J. and Lawson, W. (2000). Structural styles and deformation fields in glaciers: a review. *Geological Society, London, Special Publications* 176, 59–83. DOI: `10.1144/GSL.SP.2000.176.01.06`.

Hambrey, M. J. and Muller, F. (1978). Structures and Ice deformation in the White Glacier, Axel Heiberg Island, North West Territories, Canada. *Journal of Glaciology* 20, 41–66.

Hansen, S. (2003). From surge-type to non-surge-type behaviour: Midtre Lovenbreen, Svalbard. *Annals of Glaciology* 36, 97–102.

Harland, W. B. (1998). The Geology Of Svalbard. *The Geological Society, London,* 529 pages.

Herzfeld, U., Clarke, G., Mayer, H., and Grave, R. (2004). Derivation of deformation characteristics in fast moving glaciers. *Computers and Geosciences* 30, 291–302. DOI: `doi:10.1016/j.cageo.2003.10.012`.

Herzfeld, U. and Mayer, H. (1997). Surge of Bering Glacier and Bagley Ice Field, Alaska : an update to August 1995 and an interpretation of brittle-deformation patterns. *Journal of Glaciology* 43 (145), 427–434. URL: `http://www.igsoc.org:8080/journal/43/145/igs_journal_vol43_issue145_pg427-434.pdf`.

Holt, T. O., Glasser, N. F., Quincey, D. J., and Siegfried, M. R. (2013). Speedup and fracturing of George VI Ice Shelf, Antarctic Peninsula. *The Cryosphere* 7 (3), 797–

816. DOI: `10.5194/tc-7-797-2013`. URL: `http://www.the-cryosphere.net/7/797/2013/`.

Hooke, R. L. (2005). Principles of Glacier Mechanics. *Cambridge University Press*, 448 pp.

Hopkins, W. (1844). On the motion of glaciers. *Transactions of the Cambridge Philosophical Society* 8, 50–74.

Howat, I. M., Joughin, I., Tulaczyk, S., and Gogineni, S. (2005). Rapid retreat and acceleration of Helheim Glacier, east Greenland. *Geophysical Research Letters* 32 (22). DOI: `doi:10.1029/2005GL024737`.

Ingólfsson, Ó. (2011). Fingerprints of Quaternary glaciations on Svalbard. *Geological Society, London, Special Publications* 354, 15–31. DOI: `10.1144/SP354.2`.

Jakobsson, M., Mayer, L., Coakley, B., Dowdeswell, J. A., Forbes S. and Fridman, B., Hodnesdal H. and Noormets, R., Pedersen, R., Rebesco M. and Schenke, H. W., Zarayskaya, Y., Accettella, D., Armstrong A. and Anderson, R. M., Bienhoff, P., Camerlenghi, A., Church, I., Edwards, M., Gardner, J. V., Hall, J. K., Hell, B., Hestvik, O., Kristoffersen, Y., Marcussen, C., Mohammad, R., Mosher, D., Nghiem, S. V., Pedrosa, M. T., Travaglini, P. G., and Weatherall, P. (2012). The International Bathymetric Chart of the Arctic Ocean (IBCAO) Version 3.0. *Geophysical Research Letters* 39 (12). ISSN: 1944-8007. DOI: `10.1029/2012GL052219`. URL: `http://dx.doi.org/10.1029/2012GL052219`.

Joughin, I. and MacAyeal, D. R. (2005). Calving of large tabular icebergs from ice shelf rift systems. *Geophysical Research Letters* 32 (2). DOI: `10.1029/2004GL020978`.

Kääb, A., Lefauconnier, B., and Melvold, K. (2005). Flow field of Kronebreen, Svalbard, using repeated Landsat 7 and ASTER data. *Annals of Glaciology* 42, 7–13.

Lefauconnier, B. and Hagen, J. O. (1991). Surging and calving glaciers in eastern Svalbard. *Norsk Polarinstitutt Meddelelser* 116, 130. URL: `http://hdl.handle.net/11250/173049`.

Lefauconnier, B., Hagen, J. O., and Rudant, J. P. (1994). Flow speed and calving rate of Kongsbreen Glacier, 79N, Spitsbergen, Svalbard, using SPOT images. *Polar Research* 13, 59–65. URL: `http://www.polarresearch.net/index.php/polar/article/viewFile/6681/7514`.

Liestøl, O. (1969). Glacer surges in west Spitsbergen. *Canadian Journal of Earth Sciences* 6, 895–987. DOI: `10.1139/e69-092`.

Liew, S. C. (2015). *Principle of Remote Sensing.* URL: `http://www.crisp.nus.edu.sg/~research/tutorial/rsmain.htm` (visited on 05/06/2015).

Luckman, A., Benn, D. I., Cottier, F., Bevan, S., Nilsen, F., and Inall, M. (in review). Calving rates at tidewater glaciers depend linearly on ocean temperature. *Nature.*

Mansell, D., Luckman, A., and Murray, T. (2012). Dynamics of tidewater surge-type glaciers in northwest Svalbard. *Journal of Glaciology* 58 (207), 110–118. DOI: `doi:10.3189/2012JoG11J058`. URL: `http://www.ingentaconnect.com/content/igsoc/jog/2012/00000058/00000207/art00010`.

Meier, M. F. (1958). The mechanics of crevasse formation. *IAHS Publication* 46, 500–508. URL: `http://hydrologie.org/redbooks/a046/04646.pdf`.

Meier, M. F. and Post, A. (1987). Fast tidewater glaciers. *Journal of Geophysical Research: Solid Earth* 92 (B9), 9051–9058. DOI: `10.1029/JB092iB09p09051`.

Melvold, K. (1992). Studie av brebevegelser på Kongsvegen og Kronebreen, Svalbard (Studies of glacier dynamics on Kongsvegen and Kronebreen, Svalbard. *Rapp.ser. Naturgeogr. University of Oslo* 1.

Monteiro, L. S., Moore, T., and Hill, C. (2005). What is the accuracy of DGPS? *The Journal of Navigation* 58 (02), 207–225. DOI: `10.1017/S037346330500322X`.

Mosby, H. (1962). Water, salt, and heat balance of the North Polar Sea and of the Norwegian Sea. *Geofysiske Publikasjoner* 24, 289–313.

Mottram, R. H. and Benn, D. I. (2009). Testing crevasse-depth models: a field study at Breiðamerkurjökull, Iceland. *Journal of Glaciology* 55 (192), 746–752. DOI: `doi:10.3189/002214309789470905`.

Navarro Valero, F. J., Martín Español, A., Lapazaran Izargain, J. J., Grabiec, M., Otero García, J., Vasilenko, E., and Puczko, D. (2013). Ice volume estimates from ground-penetrating radar surveys, Wedel Jarlsberg Land glaciers, Svalbard. *In: "IASC Workshop on the dynamics and mass budget of Arctic glaciers", Obergurgl, Austria.*

Nordli, Ø. (2010). The Svalbard Airport temperature series. *Bulletin of Geography-physical geography series* (3), 5–26. URL: `http://www.apcz.pl/czasopisma/index.php/BOGPGS/article/viewFile/2326/2308`.

Norwegian Polar Institute (2015a). *Surface Material Map of Svalbard.* URL: `http://www.npolar.no/npcms/export/sites/np/images/kart/map-svalbard-surface-material-2000000.jpg` (visited on 05/07/2015).

Norwegian Polar Institute (2015b). *Topo Svalbard.* URL: `http://toposvalbard.npolar.no/` (visited on 05/07/2015).

Nuth, C., Hagen, J. O., and Kohler, J. (2015). "Geoscience Atlas of Svalbard". Ed. by W. K. Dallmann. Tromsø: Norwegian Polar Institute. Chap. Glaciers.

Nye, J. F. (1952). The mechanics of glacier flow. *Journal of Glaciology* 2 (12), 82–93. URL: `http://www.researchgate.net/profile/John_Nye2/publication/224962689_The_mechanics_of_glacier_flow/links/004635243f41372c4e000000.pdf`.

Nye, J. F. (1955). Comments on Dr. Loewe's letter and notes on crevasses. *Journal of Glaciology* 2, 512–514.

Nye, J. F. (1957). The distribution of stress and velocity in glaciers and ice sheets. *Proceedings of the Royal Society of London Series A* 239, 113–133. DOI: `10.1098/rspa.1957.0026`.

Ottesen, D. and Dowdeswell, J. A. (2006). Assemblages of submarine landforms produced by tidewater glaciers in Svalbard. *Journal of Geophysical Research: Earth Surface* 111 (F1), 2156–2202. DOI: `10.1029/2005JF000330`. URL: `http://dx.doi.org/10.1029/2005JF000330`.

Paterson, W. (1994). The Physics of Glaciers, Third Edition. *Pergamon Press, Oxford,* 480 pp.

Powell, R. D. (1983). Glacial-marine sedimentation processes and lithofacies of temperate tidewater glacier, Glacier Bay, Alaska. In: Molnia, B.F. (Ed.), Glacial Marine Sedimentation. *Plenum Press, New York.* 185–232.

Prescott, P. R., Kenneally, J. P., and Hughes, T. J. (2003). Relating Crevassing to Non-Linear Strain in the Floating Part of Jakobshavn Isbrae, West Greenland. *Annals of Glaciology* 36, 149–156. DOI: `doi:10.3189/172756403781816392`.

Quincey, D., Copland, L., Mayer, C., Bishop, M., Luckman, A., and Belò, M. (2009). Ice velocity and climate variations for Baltoro Glacier, Pakistan. *Journal of Glaciology*

55 (194), 1061–1071. DOI: `doi:10.3189/002214309790794913`. URL: `http://www.ingentaconnect.com/content/igsoc/jog/2009/00000055/00000194/art00011`.

Rignot, E. and Kanagaratnam, P. (2006). Changes in the Velocity Structure of the Greenland Ice Sheet. *Science* 311 (5763), 986–990. DOI: `10.1126/science.1121381`.

Rignot, E., Rivera, A., and Casassa, G. (2003). Contribution of the Patagonia Icefields of South America to Sea Level Rise. *Science* 302 (5644), 434–437. DOI: `10.1126/science.1087393`.

Schubert, A., Jehle, M., Small, D., and Meier, E. (2010). Influence of Atmospheric Path Delay on the Absolute Geolocation Accuracy of TerraSAR-X High-Resolution Products. *IEEE T. Geoscience and Remote Sensing* 48 (2), 751–758. DOI: `10.1109/TGRS.2009.2036252`. URL: `http://dx.doi.org/10.1109/TGRS.2009.2036252`.

Schubert, A., Jehle, M., Small, D., and Meier, E. (2012). Mitigation of atmospheric perturbations and solid Earth movements in a TerraSAR-X time-series. *Journal of Geodesy* 86 (4), 257–270. DOI: `10.1007/s00190-011-0515-6`.

Vaughan, D. G. (1993). Relating the occurrence of crevasses to surface strain rates. *Journal of Glaciology* 39, 255–266. URL: `http://www.igsoc.org:8080/journal/39/132/igs_journal_vol39_issue132_pg255-266.pdf`.

Van der Veen, C. J. (1999b). Crevasses on glaciers. *Polar Geography* 23, 213–245. DOI: `10.1080/10889379909377677`.

Van der Veen, C. J. (1999a). Fundamentals of Glacier Dynamics. *Balkema, Rotterdam.*

Van der Veen, C. J. (1998a). Fracture mechanics approach to penetration of bottom crevasses on glaciers. *Cold Regions Science and Technology* 27, 213–223. DOI: `10.1016/S0165-232X(97)00022-0`.

Vornberger, P. L. and Whillans, I. M. (1990). Crevasse deformation and examples from Ice Stream B, Antarctica. *Journal of Glaciology* 36 (122), 3–10. URL: `http://www.igsoc.org:8080/journal/36/122/igs_journal_vol36_issue122_pg3-10.pdf`.

Whillans, I. M., M., J., and Tseng, Y.-H. (1993). Velocity pattern in a transect across ice stream B, Antarctica. *Journal of Glaciology* 39 (133), 562–572. URL: `http://www.igsoc.org:8080/journal/39/133/igs_journal_vol39_issue133_pg562-572.pdf`.

Whillans, I. M. and Merry, C. J. (2001). Analysis of a shear zone where a tractor fell into a crevasse, western side of the Ross Ice Shelf, Antarctica. *Cold Regions Science and Technology* 33 (1), 1–17. DOI: `http://dx.doi.org/10.1016/S0165-232X(01)00024-6`.